Numerical modeling of geophysical granular flows: 2. Computer simulations of plinian clouds and pyroclastic flows and surges

Sebastien Dartevelle
Michigan Technological University

William I. Rose
Michigan Technological University

John Stix
McGill University

Karim Kelfoun
Blaise-Pascal Universite

James W. Vallance
Cascade Volcano Observatory

Numerical modeling of geophysical granular flows: 2. Computer simulations of plinian clouds and pyroclastic flows and surges

Sébastien Dartevelle

Department of Geological and Mining Engineering, Michigan Technological University, 630 Dow Building, 1400 Townsend Drive, Houghton, Michigan 49931, USA

Now at Los Alamos National Laboratory, Geophysics EES–11, MS D443, Los Alamos, New Mexico 87545, USA (sdart@lanl.gov)

William I. Rose

Michigan Technological University, Department of Geological and Mining Engineering, 630 Dow Building, 1400 Townsend Drive, Houghton, Michigan 49931, USA

John Stix

Earth and Planetary Sciences, McGill University, 3450 University Street, Montreal, Quebec, Canada H3A 2A7

Karim Kelfoun

Laboratoire des Magmas et Volcans, OPGC, Blaise–Pascal Université, 5, rue Kessler, 63038 Clermont–Ferrand, France

James W. Vallance

Cascade Volcano Observatory, 1300 SE Cardinal Court, Building 10, Suite 100, Vancouver, Washington 98683, USA

[1] Geophysical granular flows display complex nonlinear, nonuniform, and unsteady rheologies, depending on the volumetric grain concentration within the flow: kinetic, kinetic-collisional, and frictional. To account for the whole spectrum of granular rheologies (and hence concentrations), we have used and further developed for geophysical-atmospheric applications a multiphase computer model initially developed by U.S. Department of Energy laboratories: (Geophysical) Multiphase Flow with Interphase Exchange. As demonstrated in this manuscript, (G)MFIX can successfully simulate a large span of pyroclastic phenomena and related processes: plinian clouds, pyroclastic flows and surges, flow transformations, and depositional processes. Plinian cloud simulations agree well with the classical plume theory and historical eruptions in the upper altitude of the cloud (H_T) versus mass flux diagram. At high mass flux ($>10^7$ kg/s), plinian clouds pulsate periodically with time because of the vertical propagations of acoustic-gravity waves within the clouds. The lowest undercooled temperature anomalies measured within the upper part of the column can be as low as -18 K, which agrees well with El Chichón and Mt. St. Helens eruptions. Vertical and horizontal speed profiles within the plinian cloud compare well with those inferred from simple plume models and from umbrella experiments. Pyroclastic flow and surge simulations show that both end-members are closely tight together; e.g., an initially diluted flow may generate a denser basal underflow, which will eventually outrun the expanded head of the flow. We further illustrate evidence of vertical and lateral flow transformation processes between diluted and concentrated flows, particularly laterally from a turbulent "maintained over time fluidized zone" near source. Our comprehensive granular rheological model and our simulations demonstrate that the main depositional process is mainly a progressive vertical aggradation.

Components: 15,254 words, 18 figures, 5 tables, 6 videos.

Keywords: plinian cloud; granular gravity currents; pyroclastic flows; granular rheologies; depositional process; turbulence.

1. Introduction

[2] In the companion paper, *Dartevelle* [2004] has shown that it is possible to mathematically formulate granular viscous dissipation effects due to the turbulent kinetic motions of grains (i.e., free flights), inelastic collisions between grains of same size, and frictional contacts between grains at high concentrations. Two granular rheological models are used: a rate-of-strain-dependent for the kinetic and kinetic-collisional behavior (i.e., fluidized granular flows) and a rate-of-strain-independent for high concentration frictional-plastic granular flows. Both models are unified through a unique stress tensor for the granular phase [*Dartevelle*, 2004]. As demonstrated herewith, multiphase flow models within the Implicit MultiField formalism [e.g., *Harlow and Amsden*, 1975; *Ishii*, 1975; *Rivard and Torrey*, 1977] and with the granular model from *Dartevelle* [2004] can successfully simulate a large spectrum of pyroclastic phenomena (e.g., plinian and coignimbrite clouds and pyroclastic surges, flows, and deposits), flow transformation processes, and depositional processes.

[3] We focus on multiphase aspects not yet modeled previously and currently subject to debates in volcanology, which are abridged as follows:

[4] 1. Are numerical multiphase models able to simulate a complete and stable plinian cloud (i.e., column and umbrella) over a long period of time into the atmosphere [e.g., *Sparks et al.*, 1997] (see section 3)? This task is difficult as it requires powerful computers able to work in parallel with ad hoc parallelized codes. The ability to properly simulate plinian clouds with multiphase flow codes also depends on the global resolution (i.e., grid size) and the exact turbulence formulation.

[5] 2. Are pyroclastic flows expanded or concentrated? In other words, how do pyroclastic flows move [e.g., *Cas and Wright*, 1988; *Druitt*, 1998; *Freundt and Bursik*, 1998; *Calder et al.*, 2000] (see section 4)? This question has never been answered by previous theoretical models as they only con-

sider one end-member of the concentration spectrum at the time (dilute or concentrated), hence imposing a priori the concentration to be expected in the flow.

[6] 3. What is the main depositional process of pyroclastic flows (i.e., en masse or progressive aggradation) [e.g., *Cas and Wright*, 1988; *Druitt*, 1998; *Freundt and Bursik*, 1998] (see section 4.2.2)? Classically, if pyroclastic flows move as high concentration plug flows, then they deposit their material by en masse freezing and the transport and deposit are essentially the same. Alternatively, if the flow is diluted and fluidized, then, as the particles rain down to form a basal flow, it progressively freezes from bottom to top. In this latter case, the whole flow is stratified, subject to sharp concentration gradients, and the deposit is diachronous.

[7] 4. Is there a continuum between pyroclastic flows and surges [e.g., *Cas and Wright*, 1988] (see section 4.2.1 and section 4.2.3)? And how does flow transformation occur?

[8] These questions will be answered in the discussion sections (section 3.2 for plinian clouds and section 4.2 for pyroclastic flows), where our numerical results will be further discussed in terms of field and remote-sensing observations.

[9] This manuscript is organized as follow. First, we present the numerical methodology, viz., the computer codes (G)MFIX (section 2.1) and the initial and boundary conditions for all our simulations (section 2.2). Second, we discuss the plinian cloud simulations, emphasizing on the validation aspect and compare with various remote-sensing data (section 3). Third, we discuss the pyroclastic flow and surge simulations in the light of the granular rheological model and previous field observations (section 4). Computer-generated movies of all the simulations can be watched. All the symbols, constants, physical parameters, and equations in this manuscript have been thoroughly defined in the companion paper [*Dartevelle*,
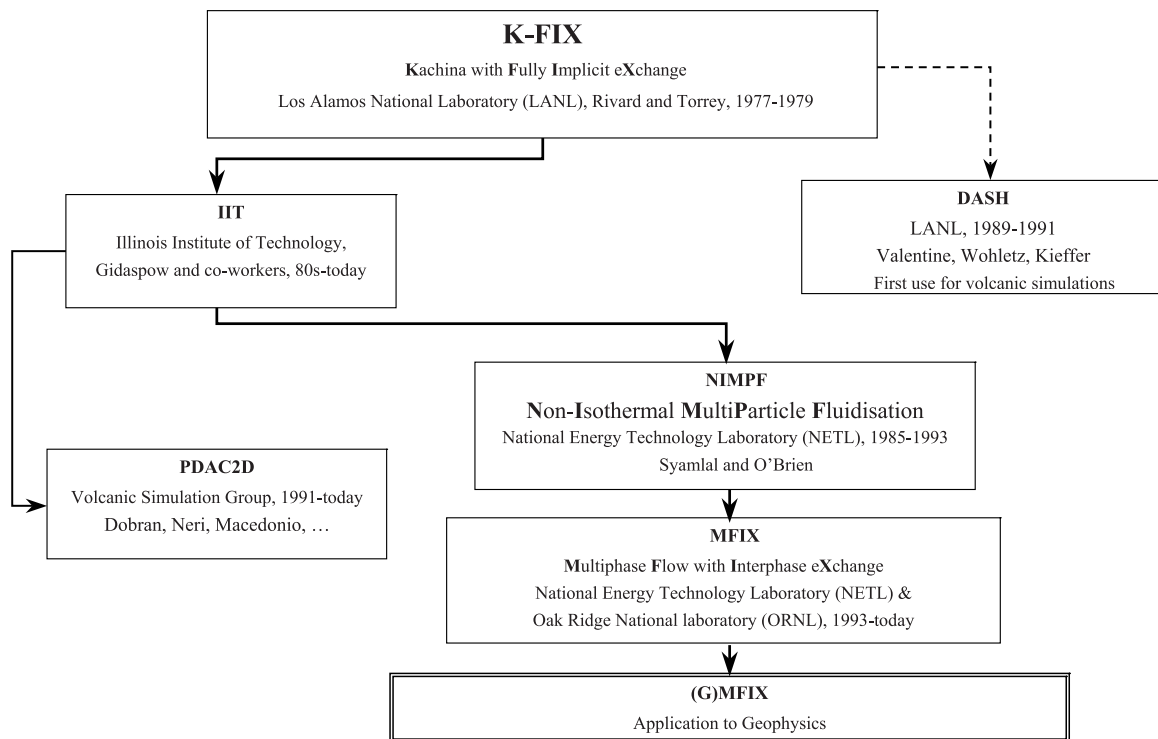
Figure 1. History of the "FIX" family computer codes used in chemical engineering, nuclear reactor dynamic, and geophysics-volcanology. For K-FIX codes, see *Rivard and Torrey* [1977, 1978, 1979] and its use in volcanology (DASH code) [e.g., see *Valentine and Wohletz*, 1989; *Valentine et al.*, 1991]; for the PDAC2D code and its earlier versions in volcanology, see, e.g., *Dobran et al.* [1993], *Neri and Macedonio* [1996], *Neri et al.* [2002], and *Todesco et al.* [2002]; for IIT and related codes, see, e.g., *Gidaspow* [1986]; for NIMPF and MFIX codes, see, e.g., *Syamlal et al.* [1993], *Syamlal* [1994, 1998], *D'Azevedo et al.* [2001], *Pannala et al.* [2003], and *Dartevelle* [2003]. The exact relationship between DASH and K-FIX is simplified as some intermediary codes may be involved (K. Wohletz, Los Alamos National Laboratory, personal communication, 2003).

2004, Appendices A and B] and will not be repeated herewith.

2. Numerical Methodology

2.1. Numerical Technique

[10] MFIX (Multiphase Flow with Interphase Exchange) is a FORTRAN 90 general purpose computer code developed at the National Energy Technology Laboratory and Oak Ridge National Laboratory for describing the hydrodynamics, heat transfer and chemical reactions in fluid-solid systems [*Syamlal et al.*, 1993; *Syamlal*, 1994, 1998]. Initially, MFIX has been adapted from the Los Alamos National Laboratory's K-FIX codes (Kachina with Fully Implicit Exchange) used to model the interaction of water and steam in a nuclear reactor [*Rivard and Torrey*, 1977, 1978, 1979]. We have adapted MFIX into a Geophysical version, (G)MFIX, in keeping all the capabilities of MFIX and adding new ones for typical geophysical-atmospheric applications (work

associated with volumetric variations of the gas phase, universal atmospheric profiles, the static *Smagorinsky* [1963, 1993] Large Eddy Simulation turbulence model, the *Zehner and Schlunder* [1970] model, the Sub-Grid turbulent Heat flux; for further details, see also *Dartevelle* [2003, 2004]).

[11] The historical relationship between MFIX, (G)MFIX, K-FIX, PDAC2D, DASH and other multiphase codes is shown on Figure 1. The "FIX" family codes have been used many times in volcanology in the past with success [e.g., *Valentine and Wohletz*, 1989; *Valentine et al.*, 1991; *Dobran et al.*, 1993; *Neri and Macedonio*, 1996; *Neri et al.*, 2002, 2003; *Todesco et al.*, 2002]. The IMF formalism adopted by the "FIX" family codes permits all degrees of coupling between the fields from very loose coupling as occurs in separated flows to very high coupling as occurs in true dispersed flows [*Harlow and Amsden*, 1975; *Ishii*, 1975; *Rivard and Torrey*, 1977; *Lakehal*, 2002]. Scalar quantities (e.g., mass, temperature, granular tem-
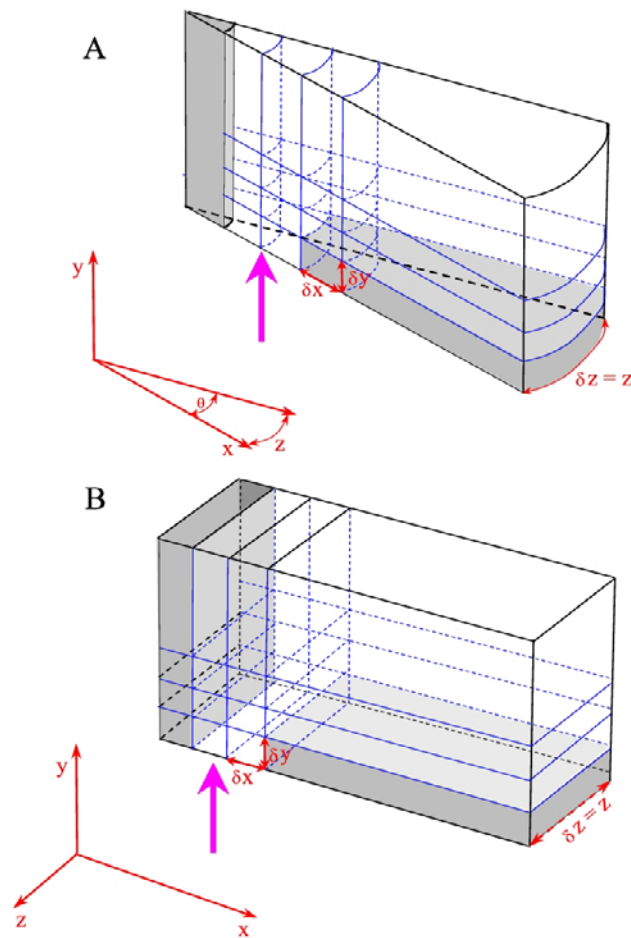
Figure 2. (a) Axisymmetric (Cylindrical) geometry for plinian cloud simulations (PL group). (b) Cartesian geometry for pyroclastic surge and flow simulations (PSF group). For both groups the vent is next to the free-slip left-side vertical wall. See Table 1a for the dimension of the computational domain. δx, δy, and δz represent the elemental length of a computational cell in the X, Y, and Z directions, respectively. As shown in these figures, all simulations are in two dimensions, which means there is no discretization along the Z direction (i.e., Z length = δz).

perature) are computed at the cell center, whereas velocity components are computed on a staggered grid coinciding with the cell boundaries [*Patankar*, 1980].

[12] The discretization of the hydrodynamic equations uses a finite volume method, which divides the physical domain into discrete three-dimensional (3-D) control volumes (i.e., cells) and then formally integrates the governing equations over them. This integration step ensures global conservation of mass, momentum, and energy independence of the grid size [*Patankar*, 1980]. (G)MFIX uses an implicit backward Euler method of time discretization and includes various first-order (e.g., FOU) and second-order (e.g., Superbee, Smart, Minmod) accurate schemes for discretizing the convection terms [*Syamlal*, 1998]. We have favored FOU (First-

Order Upwinding) for its stability, better convergence, and because we have not seen any significant differences in our geophysical simulations with the second-order schemes (such as Superbee). A detailed account of the numerical techniques can be found in Appendix B.

[13] MFIX has been extensively validated over the past years [e.g., *Boyle et al.*, 1998]. Grid-independence has been established in Fluid Cracking Catalytic risers [e.g., *Guenther and Syamlal*, 2001] and for plinian clouds simulation (see Appendix A). For pyroclastic flow simulations, the grid resolution on the ground is critical [e.g., *Dobran et al.*, 1993; *Neri et al.*, 2003] because an excessively coarse grid may simply prevent from particle settling and building a deposit. Hence careful grid size independence analysis must be achieved as shown in Appendix A.

Table 1a. Geometry, Initial and Boundary Conditions, and Various Physical Properties Used for All the Simulations[a]

Eruption	Plinian PL Group			Pyroclastic Flows and Surges PSF Group		
	PL_1	PL_2	PL_3	PF_1	PF_2	PF_3 (Inviscid)
Geometry	Cylindrical	Cylindrical	Cylindrical	Cartesian	Cartesian	Cartesian
Radial/horizontal length X, km	20	40	60	18	18	18
Radial/horizontal resolution ΔX, m	30 to 1000	50 to 1000	80 to 1000	10 to 800	10 to 800	10 to 800
Number of grid points in the X direction	145	168	150	950	950	950
Vertical length Y, km	18	25	36	10	10	10
Vertical resolution ΔY, m	30	50	80	2.5 to 1000	2.5 to 1000	2.5 to 1000
Number of grid points in the Y direction	601	501	401	95	95	95
Vent diameter/length r, m	120	400	800	100	100	100
Mixture vertical speed V_y, m/s	110	110	160	50	25	50
Volumetric solid concentration ε_s, vol.%	0.1	0.1	0.1	3.0	3.0	3.0
Grain diameter d, μm	50	50	50	250	250	250
Grain microscopic density ρ_s, kg/m³	1500	1500	1500	2500	2500	2500
Mixture temperature at the vent T_m, K	900	900	900	900	900	900
Gas pressure at the vent P_g, Pa	10^5	10^5	10^5	10^5	10^5	10^5
Mass fraction of water vapor at the vent	1.0	1.0	1.0	1.0	1.0	1.0
Calculated mixture density ρ_m, kg/m³	1.74	1.74	1.74	45.2	45.2	45.2
Calculated mass flux, kg/s	3.15×10^6	2.41×10^7	1.39×10^8	2.26×10^7	1.13×10^7	2.26×10^7

[a] See also Figure 2. In Cylindrical geometry the mass flux at the vent is calculated by $\pi.r^2.V_y.\rho_m$, where V_y is defined by equation (1) and ρ_m is defined by equation (2). In Cartesian geometry the mass flux is calculated by $r^2.V_y.\rho_m$, where r^2 is the surface area made by the dimension of a fissure-like vent along the X and Z directions (i.e., 100 m in both directions). The third dimension (Z direction) is made of only one cell; hence there is no discretization of the differential equations along Z. The length in the Z direction is 100 m in Cartesian geometry and is equal to arctg(1)·X in Cylindrical geometry, where X is the length of the domain along the X direction.

[14] All numerical data at each grid point of the physical domain were postprocessed by MATLAB® with interpolation functions to generate graphical results (snapshots and animation movies). Data sampling at specific locations within the data file were exported to spreadsheets to generate all the graphs shown in the next sections.

2.2. Initial and Boundary Conditions

[15] Plinian cloud simulations (PL group) were carried out in 2-D Cylindrical geometry, where the axis of symmetry is a vertical free-slip reflector (left sidewall, Figure 2a). The pyroclastic surge (PS) and flow (PF) simulations (PSF group) were done in a 2-D Cartesian geometry where the left-side vertical wall is a free slip wall (Figure 2b). We have favored the Cartesian geometry because, in all of our simulations, PF and PS are small events which cannot be reconciled with an axisymmetric geometry: they tend not to spread all around the volcano but they are rather channeled and they flow down drainages [*Druitt*, 1998]; that is, they flow in a specific direction. This is also the case in more important eruptions (e.g., Mt. St. Helens) and in analog experiments [*Woods and Caulfield*, 1992; *Sparks et al.*, 1997]. For all simulations, the ground is a no-slip wall, the vertical right-side and horizontal top boundaries are transient free outflow/inflow

boundaries, i.e., each scalar (P, T, ρ_g, ε, etc.) within the boundary is equal to the value of the corresponding variable within the next adjacent domain cell. Therefore these boundaries are, at any time and at any altitude, in equilibrium with the atmosphere within the flow domain. Different top boundaries have also been tested, e.g., outflow/inflow at constant pressure and temperature and free-slip wall (closed top boundary). The influence of all these boundary conditions on the global flow dynamic is very minor, which is consistent with other numerical models and previous modeling [*Neri et al.*, 2003; K. Wohletz, personal communication, 2004; unpublished data].

[16] Table 1a details the geometrical, boundary, and initial conditions for all simulations. At the vent, all simulations are carried out with (1) a constant discharge gas pressure balanced with the local atmospheric pressure, (2) thermodynamic equilibrium between gas and pyroclasts, (3) only water vapor in the erupting mixture, (4) constant mass flux at the vent throughout the whole simulation time (i.e., 1 hour for the PL group and 8 min for the PSF group), (5) within the same atmospheric environment assumed to be a dry, quiet and temperate standard atmosphere (Table 1b), and (6), for the PSF group, a nil granular temperature as an initial condition (the end result is insensitive of the

Table 1b. Identical Atmospheric Conditions for All Simulations[a]

Atmospheric Property	Value
Pressure at vent level	10^5 Pa
Temperature at vent level	298 K
Calculated gas density at vent level	1.169 kg/m^3
Vapor mixing ratio at vent level	0 (dry atmosphere)
Tropospheric temperature gradient (0–11 km)	−7 K/km (temperate atmosphere)
Lower stratospheric temperature gradient (19–32 km)	+1.8 K/km
Upper stratospheric temperature gradient (32–47 km)	+2.8 K/km
Tropopause	11–19 km

[a] A temperate, dry, idle standard atmosphere.

initial value chosen for the granular temperature). "Vent diameter or vent length" must be understood as the diameter/length measured exactly where the mixture is not bounded anymore by a vertical wall. For instance, in PL_3 simulation (Table 1a), the large diameter of 800 m can be interpreted as the one of a large crater as seen in the 1990 Lascar eruption (which had a 1200 m diameter) [*Sparks et al.*, 1997].

[17] From Table 1a, the only difference between the simulation of a given group is the initial mass flux at the vent. Within the PL group, there is about a factor of ten between each plinian simulation, while within the PSF group, there is a factor two between PF_1 and PF_2 simulation. In order to compare the benefits of a comprehensive granular rheological model, we have performed a third simulation (PF_3) in which the granular phase is assumed to be inviscid and compared with an identical simulation (PF_1, same initial/boundary conditions) which has a full kinetic-collisional-plastic formulation.

[18] These grid size configurations were mostly prescribed by our available computer resources. For the PL group, the overall size of the computational domain has been chosen to ensure that the whole plinian flow would remain inside the domain in order to capture the entire plinian activity (column, umbrella, shape, temperature anomalies) and to capture, with the best possible resolution possible, the column, its edges, and the transition between the jet, the buoyant column and the umbrella. The grid size is uniform along the vertical direction and slowly increases radially away from the axis of symmetry. For the PSF simulations, the grid size is thoroughly nonuniform over the whole computational domain with the highest horizontal resolution on the left-side (10 m over a horizontal distance of 9 km) and the highest vertical resolution at the ground (2.5 m over a height of 100 m). This resolution configuration has been chosen to enable us to capture flow trans-

formations, sedimentation, depositional processes and to capture the exact relationship between PF and PS. Grid size analysis and grid size effects is further detailed in Appendix A.

[19] We do not claim to comprehensively simulate "real" plinian clouds or pyroclastic flows and surges with this limited set of initial and boundary conditions and with the limitation of our mathematical model [*Dartevelle*, 2004]. Instead, we humbly aim (at this stage) to reproduce some of the known or expected physics of those volcanic events. Specifically, in this manuscript, we would like to demonstrate the importance of granular rheologies to capture some well-known features of PF and PS (e.g., formation of the deposit, outrun of the dilute part of flow by a more concentrated PF, lateral and vertical flow transformation processes) and demonstrate that multiphase flow models can simulate some of the well-known features of plinian clouds (column and umbrella).

[20] We have carried out all our simulations with only one particle size because we wanted to keep the complexity of the model as "low" as possible in order to capture only the fundamental physics of our rheological model (more grain sizes would have implied supplementary assumptions and constitutive equations). Of course, natural granular flows are multisized which may have important effects upon flow dynamics [e.g., *Neri and Macedonio*, 1996; *Neri et al.*, 2003]. Yet such supplementary complexity would have obscured (at this stage) the underlying physics behind granular rheologies. In the long run, supplementary particle sizes may be introduced in our model. In the same vein, the boundary condition at the ground is a flat surface because 2-D topography would not have added anything relevant to our current modeling objectives.

[21] In the following, we define the mean mixture value of a given variable (Ψ) such as speed (U_x or V_y) or temperature (T_m) and the mean mixture
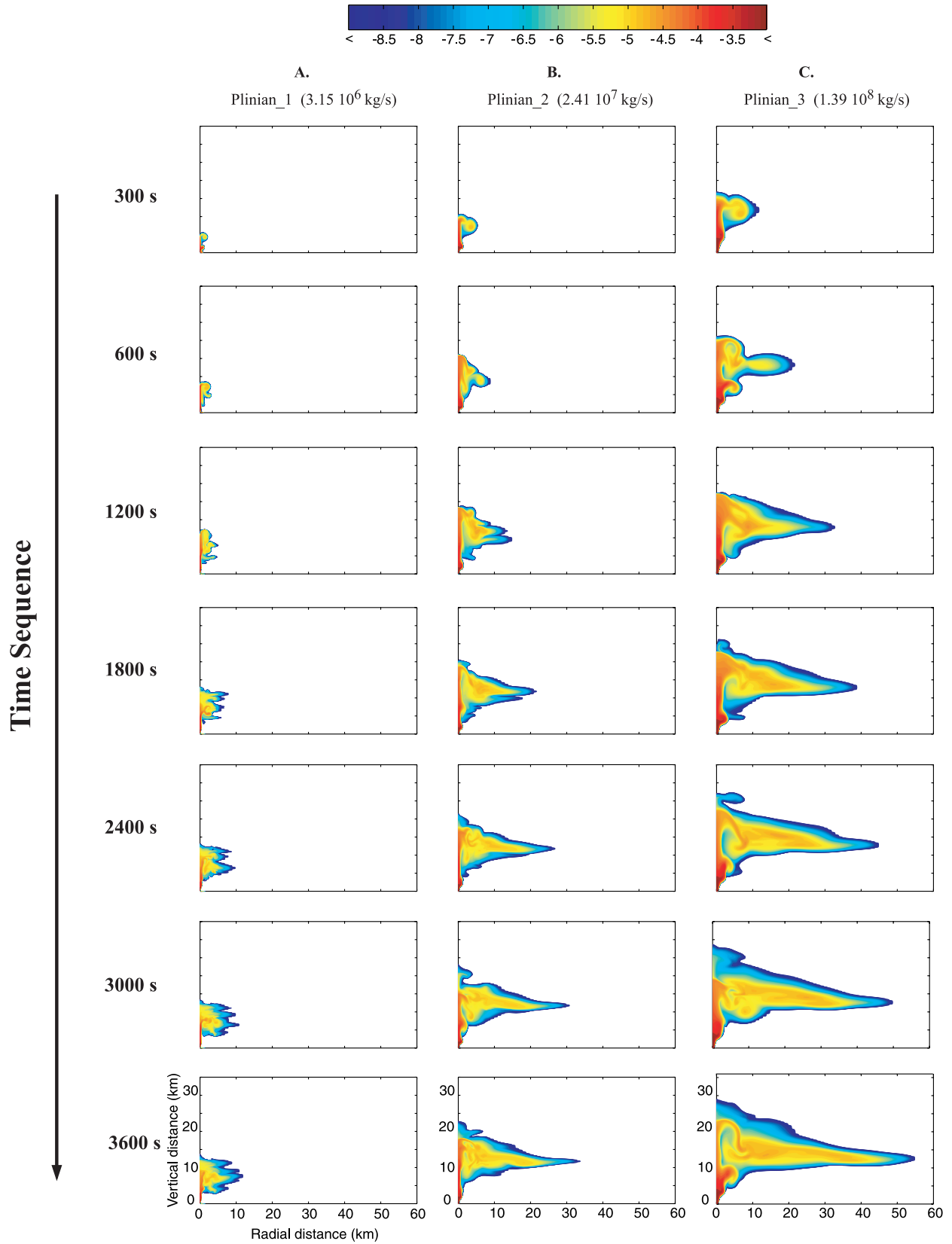
Geochemistry
Geophysics
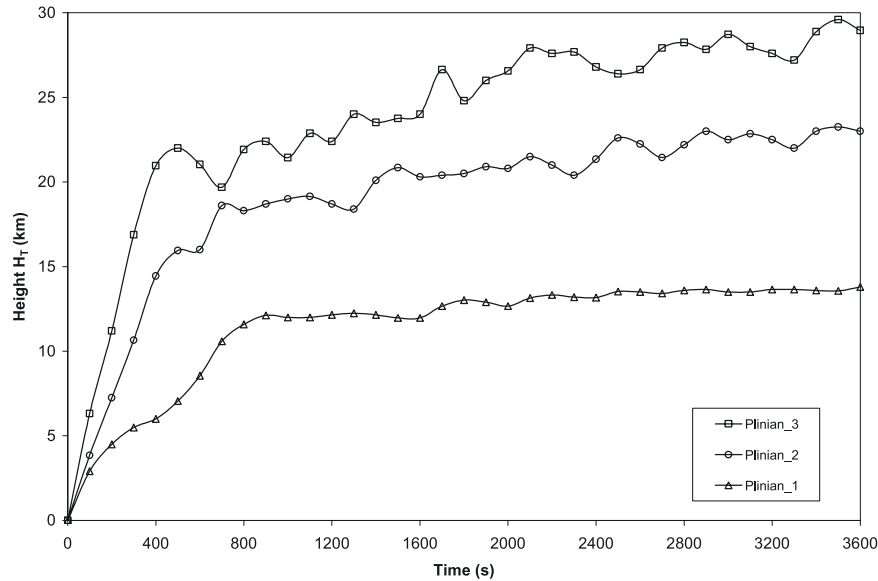Geosystems
G^3

Figure 3

Figure 4.   Variation of the top altitude of the column (H_T) with time (between 0 and 3600 s) for the three plinian column simulations. Note the fluctuating and pulsating behavior of PL_2 and PL_3 clouds with time.

density (ρ_m) as [*Valentine and Wohletz*, 1989; *Dobran et al.*, 1993]:

$$\Psi = \frac{\varepsilon_s \rho_s \Psi_s + \varepsilon_g \rho_g \Psi_g}{\rho_m}, \tag{1}$$

$$\rho_m = \varepsilon_s \rho_s + \varepsilon_g \rho_g, \tag{2}$$

where ψ_s and ψ_g are the corresponding variable of a given phase (all other symbols are defined in the Appendix A of *Dartevelle* [2004]).

3. Plinian Cloud Modeling

[22] Figure 3 represents various snapshots of the logarithm of the volumetric grain concentration, $\log_{10}(\varepsilon_s)$ (from 10^{-2} to 10^{-9}), taken at different times (from 300 s to 3600 s) for three plinian simulations. Figure 4 represents the altitude of the top (H_T) of the plinian column versus time. The following description is also based on the computer-generated movies of three plinian simulation

(Movie 1 to Movie 3 for simulation PL_1 to PL_3, respectively).

3.1. General Descriptions

[23] First, simulation PL_1 ("small" eruption, $\sim 10^6$ kg/s). The jet part is quickly decelerated to an altitude of about 1 km from which a rising buoyant convective plume develops. At 200 s, the plume has reached an altitude of 4.5 km (Figure 4). At that time, a partial collapse of the system occurs at the transition between the jet and lower part of the plume, forming small pyroclastic flows (Movie 1). This partial collapse drastically reduces the growth of the column (Figure 4). Once the system is relieved from this excess of materials (400 s), the plume regains enough buoyancy to move upward to higher altitudes. At 2400 s, the whole plinian system stabilizes over time and gently spreads radially with no noticeable change of H_T. Within an hour, H_T is about 13.5 km and the maximal radial distance is about 12 km. The umbrella is clearly sheared as the mixture mean radial speed (U_x)

Figure 3.   Time sequence over 1 hour of three plinian clouds. The color code represents the logarithm of the volumetric solid concentration ($\log_{10}\varepsilon_s$): the redder, the more concentrated; the bluer, the more diluted (the blue atmosphere has initially no grains). (a) Simulation PL_1 (3.15×10^6 kg/s). (b) Simulation PL_2 (2.41×10^7 kg/s). (c) Simulation PL_3 (1.39×10^8 kg/s). It is worth noting the heterogeneity in grain volumetric concentration throughout the whole plinian flow (column and umbrella) and the very low grain concentration veil at the top of the plinian column and surrounding its umbrella.
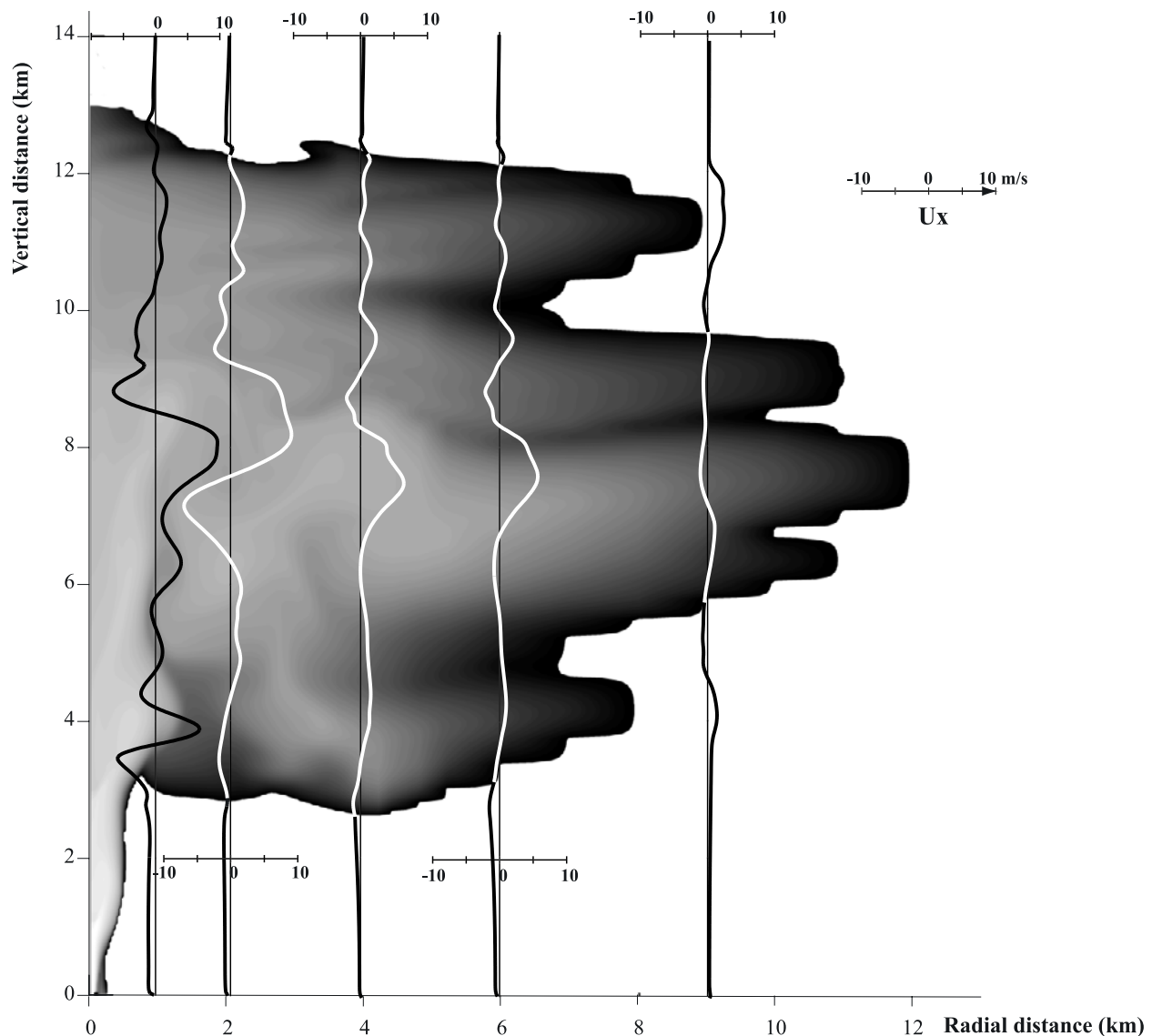
Figure 5. Radial speed profiles (U_x in m/s) along the vertical direction (between 0 and 14 km) at different radial positions within the plinian cloud for simulation PL_1. The gray background color of the cloud represents the intensity of volumetric solid concentration gradient in any direction (the steeper the gradient, the darker). Note backward radial draughts shearing the umbrella, which explains its finger-like morphology.

shows very complex backward and forward profiles (Figure 5). For instance, after one hour, at a radial distance of 6 km, backward currents are well-developed at an altitude of 6, 9, and 10 km, which explains this fingering shape. Also, note the systematic backward current at the bottom of the umbrella.

[24] From Movie 1, turbulence and eddy developments are the most active between a radial distance of 1 and 2 km, i.e., within the transitional zone between the column and the umbrella. This explains the complex radial speed profiles at a distance of 1 km in Figure 5 where an important entrainment of air in the column between an altitude of 2 and 3.8 km and reentrainment of pyroclastic materials to the column at higher altitudes occurs (e.g., at altitudes of 4.4, 5.5 km, and between 8.5 and 10 km). These radial speed profiles, backward currents within the umbrella, and multilayered umbrellas are in a qualitative agreement with the experimental observations of *Holasek et al.* [1996]. However, in PL_1 simulation, it can be seen from Figure 3 and Movie 1 that multiumbrellas are formed very early as the column rises in the atmosphere. In addition, their
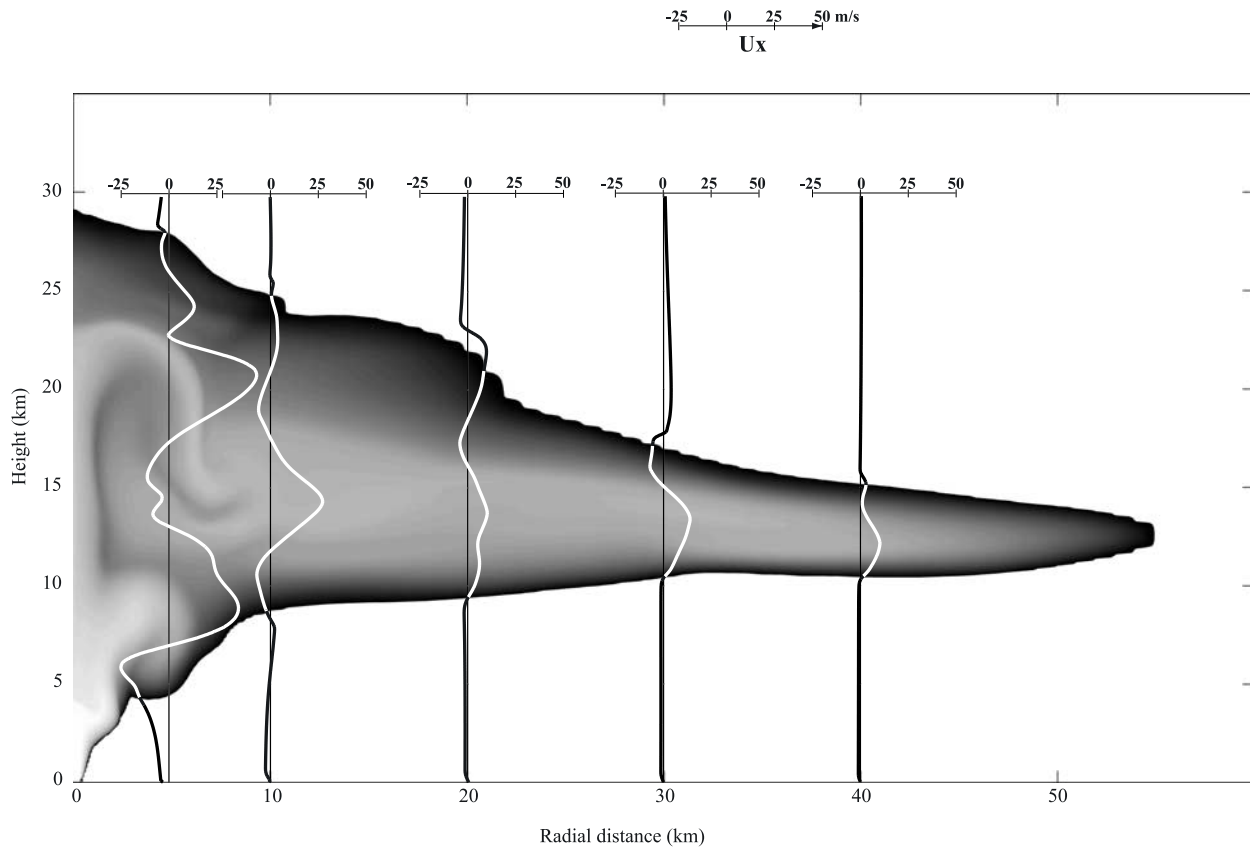
Figure 6. Radial speed profiles (U_x in m/s) along the vertical direction (between 0 and 30 km) at different radial positions within the plinian cloud for simulation PL_3. Same gray background color as in Figure 5.

development is strongly dependent on the exact state of turbulence and eddies within the clouds. Hence the multilayered umbrellas are caused by the nonlinear dynamics within the clouds and cannot solely be attributed to a secondary sedimentation of particles along the edges of the column from another, higher up, preexisting umbrella as suggested by *Holasek et al.* [1996].

[25] Second, the simulation PL_3 which has a mass flux ~100 times higher than PL_1 (i.e., ~10^8 kg/s). Because the jet suffers strong deceleration while ''pushing'' against the atmosphere, it converts nearly all its initial kinetic energy into heat. Hence the top of the jet is characterized by much higher pressure than the ambient (e.g., after 3600 s, it has an excess of 15 hPa at 2.4 km) [*Valentine and Wohletz*, 1989]. Above the top overpressurized jet, the plume drastically expands and accelerates outward (altitude 4 km in Figure 3c). It therefore reduces its density and becomes positively buoyant (e.g., note the ''bulgy'' shape of the column above the jet between 4 and 6 km in Figure 3c). At 300 s, the plume has reached an altitude of ~17 km (see Figure 4) and starts to spread laterally to form an

umbrella. However, the plume is still moving upward to an altitude of 22 km owing to its inertia. In Figure 3c (600 s), the top of the column is therefore 5 km higher (i.e., 21 km) than the umbrella which lies between 12 and 16 km. Afterward, the column is gently growing to higher altitudes with the formation of secondary diluted clouds topping the column itself (see Figure 3c at 2400 s and Movie 3). After one hour, the plinian column has reached a maximum altitude of about 29 km and a radial distance of about 52 km.

[26] Figure 6 represents radial speed profiles along the vertical direction measured at different positions after one hour. Again, the umbrella is clearly sheared. It has a well-developed positive radial speed of 26 m/s at 10 km decreasing to less than 10 m/s at 40 km away from source. U_x tends to be maximum in the central part of the umbrella and to be negative at the top and bottom where friction with the atmosphere is maximum. Because of the active turbulent area between the column and umbrella (e.g., at a radial position of 5 km), U_x shows complex back and forth speed profiles with an important entrainment of fresh air at the bottom

of the column, specially where it expands the most (between 4 and 7 km of altitude).

[27] Figure 7 shows V_y profiles taken after one hour at different heights within PL_3 cloud. At an altitude of 1 km within the jet, V_y has a classical Gaussian shape profile where V_y is maximum at the center of the column and exponentially decreases toward the edges. At 4 km, at about the transition between the jet-plume, V_y tends to be minimal at the center of the column and maximal at the edges where entrainment is the most active. This is consistent with negative U_x profile at the bottom just next to the column as in Figure 6. At 6 km, V_y is positive along the whole radial direction (from center to edges) owing to the cloud expansion and the active entrainment of fresh air. At higher altitude vertical speed profiles tend again to Gaussian profiles, although disturbed by turbulence, reentrainment, and the formation of vertical convective supercells between the plume and the umbrella.

[28] As noted by *Dobran et al.* [1993] and as seen in Figure 8, it is difficult to determine exactly the transition between the strongly thrusting jet and the buoyant plume itself. Figure 8 shows the variation along the vertical direction inside the plinian column PL_3, at time 3600 s, of the averaged mixture temperature (Figure 8a), the pressure anomaly relative the ambient (Figure 8b), the averaged mixture vertical speed (Figure 8c), and the density differences relative to the ambient (Figure 8d) of the macroscopic gas phase density ($\Delta\rho_g$, dashed curve) and the macroscopic solid phase density ($\Delta\rho_s$, plain curve) of the column. Just above the vent (80 m), the jet is overpressured relative to the ambient (+59 hPa, not seen on Figure 8b) which is also shown by a slight decrease in V_y owing to the conversion of kinetic energy into pressure. Higher up, the jet tends to reequilibrate with the ambient showing a sharp decrease in ΔP_g (down to +0.96 hP) and a slight increase in V_y. The thrusting decelerating jet into the atmosphere causes a second pressure maximum (+15 hPa) at a height of 2.4 km suggesting a classical flaring characteristics or diamond-like structure of overpressured jets [*Valentine and Wohletz*, 1989]. At 3.9 km, ΔP_g decreases to a negative value (decompression) down to −12 hPa, hence the column expands, which drastically reduces the density of the system in making the solid phase positively buoyant relative to the ambient (Figure 8d). The expansion of the system also reduces the temperature by nearly 200 K (Figure 8a), hence causing a slight

decrease in buoyancy of the gas phase (Figure 8d). Owing to the inertia of the jet, at a height of 3.9 km, V_y is minimum at the center of the column while at its edges, V_y is ∼+73 m/s. The radially fast expanding system and the sharp increase of buoyancy cause the system to reaccelerate upward and outward from slightly less than 0 m/s to 80 m/s at 6.4 km causing a third maximum in ΔP_g at ∼9.8 km. Clearly, between the top of the thrusting jet and the fully buoyant plume, there is a transitional zone which extends between the second maximum in pressure (altitude 2.4 km) and the altitude of full positive buoyancy (i.e., 3.9 km).

[29] The intermediate plinian simulation (PL_2) presents very similar features as PL_3 (see Movie 2 and Figure 3b). The transition between the jet and the plume is at about 2 km with a well developed "swelling" at the top of the jet owing to the expansion of the plume. Both PL_2 and PL_3 simulations clearly show a pulsating behavior with time (see Movie 2, Movie 3, and Figure 4).

3.2. Discussion

3.2.1. Top Altitude Versus Mass Flux

[30] Plinian column upper heights (H_T) have been often related to the mass flux at the vent because this flux represents the amount of energy released and available to the plinian column. Figure 9 represents H_T of the plinian column versus the inferred mass flux at the vent for different historical eruptions and our plinian simulations (PL_1, PL_2, and PL_3) where H_T is measured at 3600 s. Also shown on Figure 9, the best fit curve between the past eruptions [*Wilson et al.*, 1978; *Settle*, 1978; *Sparks et al.*, 1997] and two curves from *Morton et al.*'s [1956] theory for two temperatures at the vent [from *Wilson et al.*, 1978]. Knowing the uncertainties for historical eruptions to infer the exact H_T and, most importantly, the mass flux at the vent, the top altitude predicted by our model is in excellent agreement with past eruptions and quite surprisingly with *Morton et al.* [1956] theory which was initially developed for plume within the troposphere only [*Sparks*, 1986]. From Figure 9, we may conclude that (G)MFIX model can accurately be compared with classical plume theory [e.g., *Morton et al.*, 1956; *Wilson et al.*, 1978; *Sparks*, 1986] and most importantly real observations.

3.2.2. Temperature Anomalies

[31] Temperature anomalies at the top of the column are important features to capture as they can
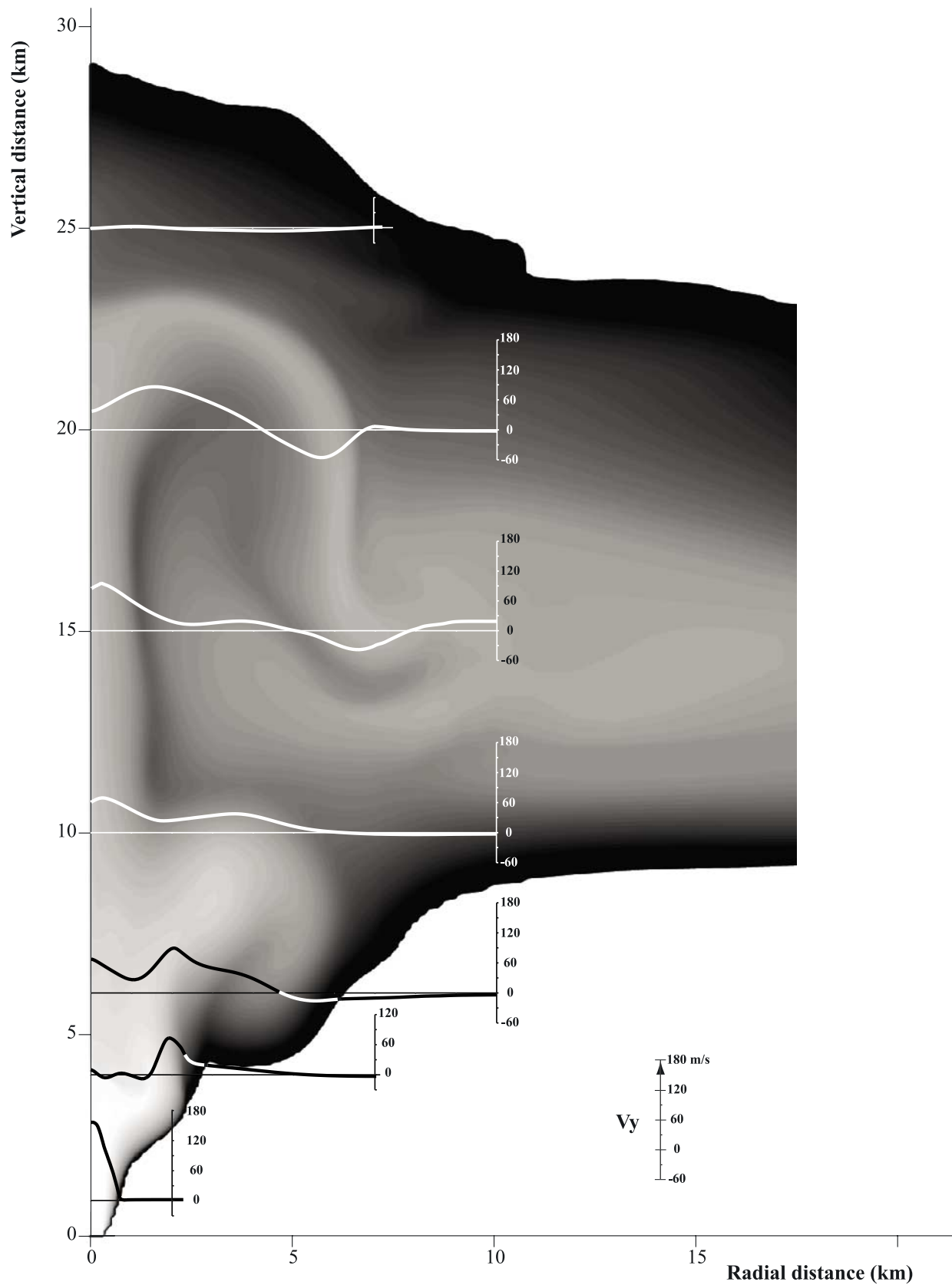
Figure 7. Vertical speed profiles (V_y in m/s) along the radial direction (between 0 and 10 km) at different altitudes within the plinian cloud for simulation PL_3. Same gray background color as in Figure 5.
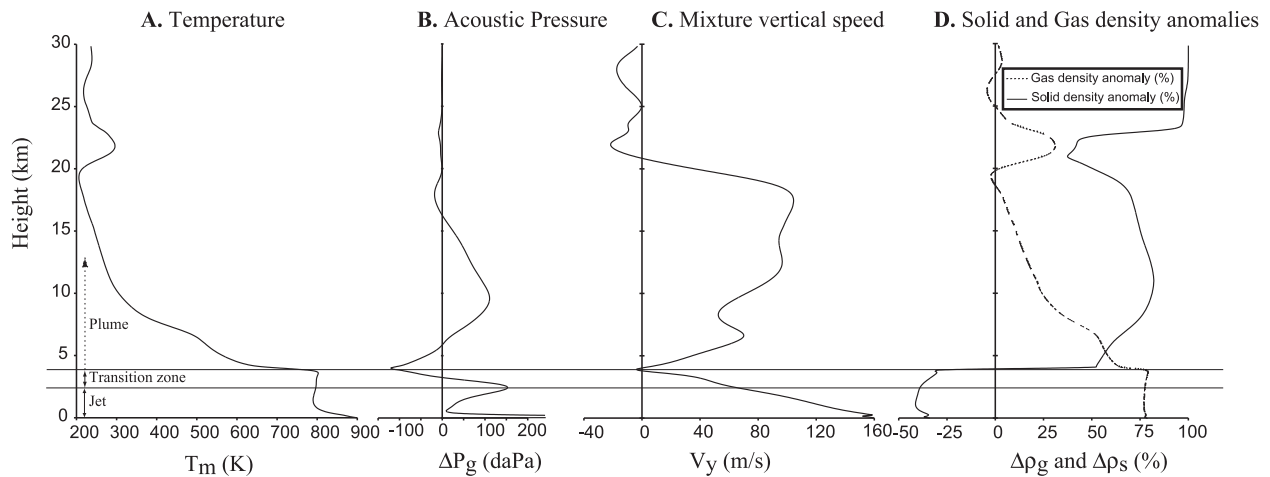
Profiles in the plinian column PL_3 at 3600 s

Figure 8. Vertical profiles within the plinian column PL_3 taken at 3600 s. (a) Averaged mixture temperature (T_m in K) calculated by equation (1). (b) Acoustic pressure: difference between the gas pressure inside the column and the undisturbed atmospheric pressure ($\Delta P_g = P_g - P_{atm}$ in daPa, where 100 daPa = 1000 and Pa = 10 hPa). (c) Averaged mixture vertical speed (V_y in m/s). (d) Density anomalies: difference between the atmospheric density and the gas macroscopic density within the column ($\Delta \rho_g = 1 - \varepsilon_g \rho_g / \rho_{atm}$) or the solid macroscopic density ($\Delta \rho_s = 1 - \varepsilon_s \rho_s / \rho_{atm}$) within the plinian column (in %). Note at 3.9 km, where the system is expanding the most, the sharp decrease of temperature (by nearly 200 K), hence the slight decrease of buoyancy of the gas phase but the dramatic increase of buoyancy of the solid phase (dilution).

be inferred by satellite remote sensors. This would provide a supplementary way to compare with real data. Figure 10 and Movie 4 show the temperature anomalies relative to the ambient (ΔT) versus time for the simulation PL_3. In Figure 10, we match H_T variation with ΔT measured at the "tip of the top" of the plinian column. During the early stages, the column rises into the atmosphere where the ambient pressure decreases, hence the column expands which causes a sharp decrease of temperature at the top of the column: at 500 s and a height of 22 km, the top of the column is undercooled relative to the ambient by 11 K. As the column drops (to 19.6 km at 700 s), the column contracts and adiabatically warms up (+19 K). Since the column PL_3 has a natural tendency to pulsate, H_T changes with time, so does ΔT (Figure 10). From Movie 4, these temperature anomalies can be seen throughout the whole cloud. In particular, vertical convective supercells are developed between the column and the umbrella where the downdraughts and updraughts are warmer and colder, respectively, than the ambient.

[32] *Holasek and Self* [1995] have measured temperature anomalies between −6 K and −15 K in Mt. St. Helens plume and, for El Chichón, *Woods and Self* [1992] have inferred temperature anomalies as low as −20 K. Those data match very well

with the −11 K measured at the "tip of top" of our simulated plinian column (PL_2 and PL_3), but also with the temperature anomalies deeper inside the PL_3 column which are as low as −18 K (not shown on Figure 10). Simulation PL_2 shows the same trend of ΔT variations at the top of the column but within a smaller temperature span (−9 K and +15 K). Simulation PL_1 only shows small temperature anomalies as it rises in the atmosphere (−10 K) and after 500 s, the top of the cloud has the same temperature as the ambient.

3.2.3. Nonuniform Clouds and Remote Sensors

[33] A close inspection of the umbrellas in Figure 3, Movie 1, Movie 2, and Movie 3 suggests that plinian clouds are very heterogeneous in terms of the volumetric solid concentrations both in time and space (vertical and lateral variations), even far away from the column. This is an important result for remote-sensing techniques which assume the cloud is somehow homogenous within the pixel where measurement is carried out. For instance, the retrieval of sizes and particle burden within volcanic clouds with the AVHRR band 4 and 5 [*Wen and Rose*, 1994] relies on a perfectly homogenous single layer umbrella, which is not the case in Figure 3a (multilayered umbrellas) or Figure 3b
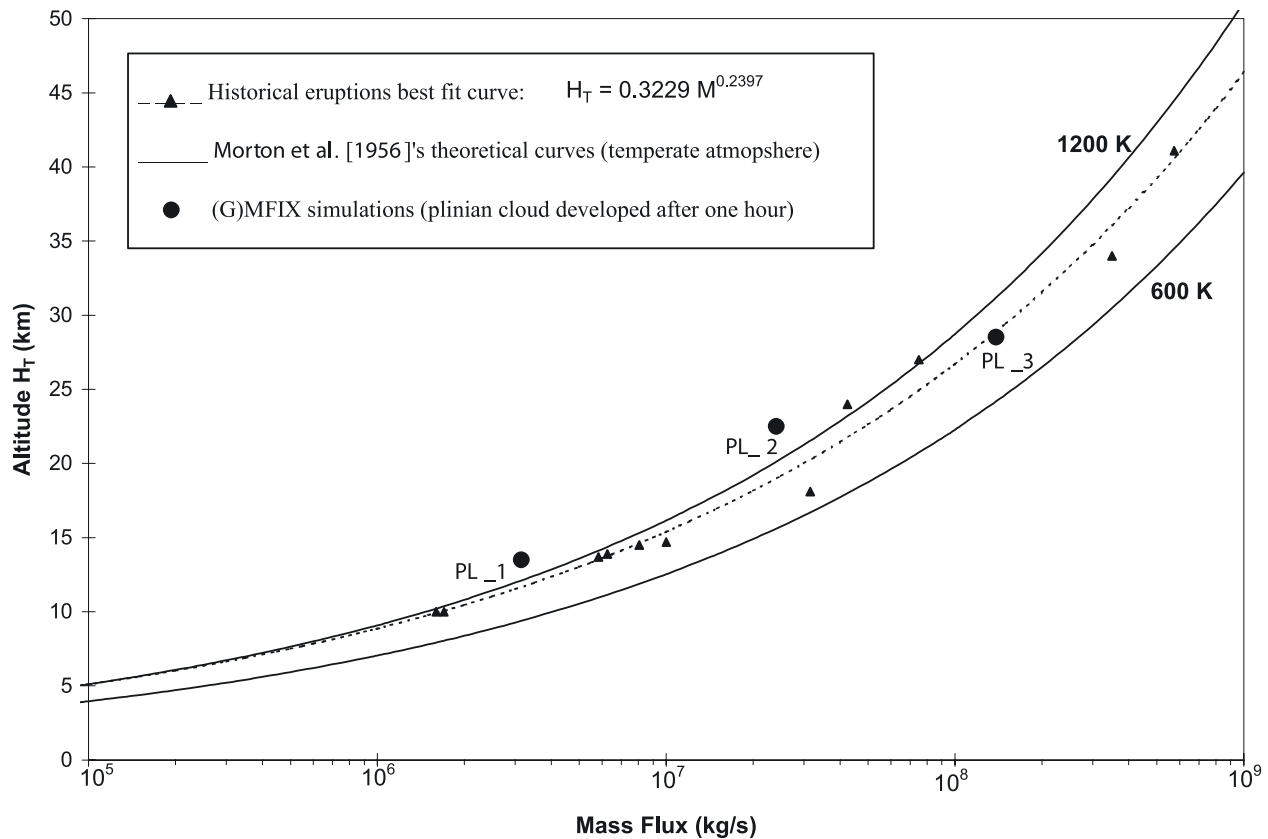
Figure 9. Top altitude of the plinian cloud (H_T in km) versus mass flux at the volcanic vent (kg/s). Triangles are for historical eruptions from which H_T and the mass flux have been inferred from field studies and remote-sensing observations (i.e., not inferred by some previous modeling) (data from *Wilson et al.* [1978], *Settle* [1978], and *Sparks et al.* [1997]); the dashed curve is the best regression fit between these historical eruption data; the plain curves are from the *Morton et al.* [1956] theory calculated for two initial magma temperatures at the vent (600 K and 1200 K); and the circles are for (G)MFIX's three plinian simulations. Knowing all the uncertainties of historical eruptions for determining the mass flux at the vent and H_T, we may conclude that there is an excellent agreement between (G)MFIX's simulations and past historical eruptions.

and Figure 3c, which show complex concentration profiles within the first 10 to 20 km from the source. Another widely used remote-sensing technique like cloud temperature retrieval relies on a fully opaque and homogenous cloud where it is the densest [*Sparks et al.*, 1997]. However, it is well-known [*Sparks et al.*, 1997] that plumes present at their tops low ash concentrations regions, which is fully confirmed by our numerical models (Figure 3 for all three plinian simulations). Consequently, the factual temperature measured by remote sensors is at an undetermined depth within the plume where it becomes fully opaque and is not necessarily measured at the "tip of the top" of the plume (as shown in Figure 10). Hopefully, in a near future, multiphase flow modeling will provide further useful hints about the nonuniformity of plinian clouds which may eventually help for the development of

better and more accurate retrieval remote-sensing algorithms.

3.2.4. Unsteady Clouds

[34] Strong plinian columns tend to be highly unsteady and pulsate with time [*Rose et al.*, 1995; *Zurn and Widmer*, 1996; *Tahira et al.*, 1996; *Johnson*, 2003]. This unsteady behavior is also well known by field volcanologists who have observed that many plinian fall deposits exhibit variation in particle size as a function of the stratigraphic height. Usually, reverse grading is more common and is interpreted as due to an increasing eruption intensity with time [*Cas and Wright*, 1988; *Sparks et al.*, 1997]. That is exactly what is shown for PL_3 in Figure 4 and Figure 10, where, at 700 s, the altitude is 19.8 km and within
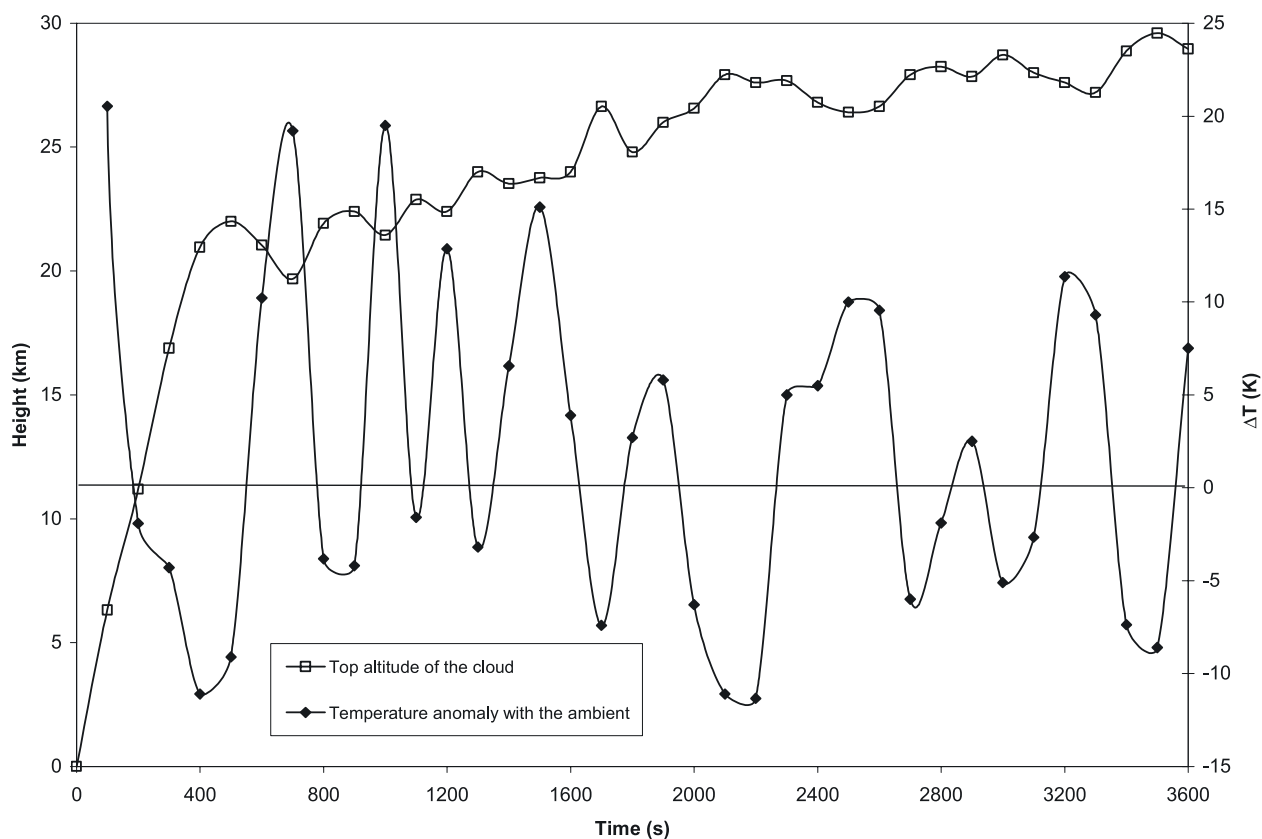
Figure 10. Top height of the PL_3 cloud (H_T, left vertical axis) and temperature anomalies at the top of the cloud relative to the ambient ($\Delta T = T_m - T_{atm}$, right vertical axis) versus time (between 0 and 3600 s). The horizontal line represents $\Delta T = 0$ K.

the next 2900 s the altitude increases to about 29 km. It is even possible that PL_3 cloud has not yet reached its maximum altitude after one hour of simulation.

[35] Another interesting feature of plinian simulations PL_2 and PL_3 are the small vertical bursts and pulsations of the column of about ±1 to 3 km and with a periodicity of about 5 min (Figure 4, Figure 10, and Movie 2 to Movie 4). *Rose et al.* [1995], using real-time radar observations, showed that the altitude of Crater Peak September 12, 1992 eruption column fluctuated within ±2 km, which is consistent with our simulations. Such vertical gravity-acoustic waves as seen in Movie 2 and Movie 3 are also well-confirmed by measurement of acoustic and worldwide Rayleigh waves generated by powerful eruptions [e.g., *Zurn and Widmer*, 1996; *Tahira et al.*, 1996; *Johnson*, 2003]. Typically, in the cases of strong eruptions such as Mt. St. Helens [*Mikumo and Bolt*, 1985] and Mt. Pinatubo [*Tahira et al.*, 1996; *Zurn and Widmer*, 1996], more than 10 hPa of pressure anomalies with a periodicity of a few minutes have been measured. The magnitude of those measured pressure anomalies are also

confirmed by our simulations as seen in Figure 8b. Those vertical acoustic-gravity waves are recognized as a positive feedback, self-organized, and self-excited natural oscillator [*Zurn and Widmer*, 1996]. For instance, the rising and expansion of the plume within the atmosphere excites a large spectrum of acoustic and gravity waves (i.e., plume forcing of the atmosphere). On the other hand, the plume experiences harmonically varying buoyancy forces which makes the plume fluctuate in height (i.e., atmosphere forcing of the plume). This latter forcing is caused by harmonic pressure fluctuation within the plume and by the difference between compressibility of the atmosphere and the plume [*Zurn and Widmer*, 1996]. In addition, such an effect may be enhanced by the unsteadiness and nonuniform compressibility of the plume. These harmonic variations of the plume will again trigger new acoustic and gravity waves (positive feedback).

[36] Our simulations suggest that these periodic fluctuations as well as the global progressive increase in altitude of the column should not be ipso facto interpreted as variations at the vent level (e.g., widening of the vent, V_y or mass flux

variations) but should rather be seen as an inner, nonlinear, and chaotic feature of strong plinian clouds. In all our simulations, the vent conditions were maintained constant over the whole simulation time. Clearly, from Movie 3, it can be seen that the trigger mechanism of the gravity-acoustic waves is the pressure anomalies between the jet and the plume and not any oscillating phenomena inside the volcano. Our results are in complete agreement with the observation of *Zurn and Widmer* [1996] for the 1991 climactic eruption of Mt. Pinatubo.

[37] This is a new aspect of the physics of the plinian cloud dynamics, which has never been modeled before. It also confirms the significance of pressure anomalies for the control of the dynamic of the plinian cloud and therefore confirms the importance of including such phenomenon in an ad hoc mathematical model [*Valentine and Wohletz*, 1989].

4. Pyroclastic Flow and Surge Modeling

[38] In Figure 4 of the companion paper, *Dartevelle* [2004] has shown that the granular rheological behavior and the coupling with the gas phase turbulence are deeply dependent on the volumetric grain concentrations (ε_s). It is possible to recognize different regimes which overlap each other. First, the purely kinetic regime for very dilute suspension ($\varepsilon_s < \sim 10^{-3}$ vol.%) where collisions do not occur, the granular temperature tends to be maximized, and so does the granular shear viscosity. Second, the transitional kinetic-collisional regime, $10^{-3} < \varepsilon_s < 1$ vol.%, collisions progressively become more and more important so that the granular temperature is decreased, and so is the shear viscosity. Third, the predominantly collisional regime, $1 < \varepsilon_s < 50$ vol.%, collisions are predominant so that the granular temperature is decreased to negligible values (because of inelastic collisions), and the granular shear viscosity has reached a minimum. Fourth, the frictional regime, $\varepsilon_s > 50$ vol.%, the plastic behavior becomes more and more predominant, hence shear frictional viscosity asymptotically goes to infinity, so does the strength of the granular material, and at $\sim$64 wt.% (the maximum possible volumetric concentration for a randomly packed structures), the granular "flow" freezes (i.e., granular deposit). Hence, in this view, friction only acts as a physical process between the collisional flowing regime and a static deposit.

[39] Following *Sparks et al.* [1997], the pyroclastic surges belong in the kinetic and kinetic-collisional regime (i.e., $\varepsilon_s \ll 1$ vol.%), where the random chaotic kinetic motion of grains is the dominant mechanism of momentum and energy transfer between sheared layers. Pyroclastic flows belong to the predominantly collisional and plastic-frictional regime ($1 < \varepsilon_s < 60$ vol.%). Hence pyroclastic flows cover a quite appreciable range of volumetric grain concentrations and can be still seen as partially fluidized flows in their low concentration range.

[40] In the interpretation of our numerical results (PF_1, PF_2, and PF_3), we will only focus on four themes: (1) relative dynamic behavior between PS and PF and flow transformation, (2) formation of a deposit, (3) dynamics close to the source, and (4) the relevance of a nonlinear rheological model for granular flows (viscous or inviscid). Figure 11 and Figure 12 show the development of PF/PS over 8 min for simulations PF_1 and PF_2, respectively. Each curve represents a solid volumetric iso-concentration contour line between 10^{-9} and 10^{-1}. Movie 5 and Movie 6 show the development of the PF_1 and PF_2 simulations, respectively. Figure 13 (PF_1) and Figure 14 (PF_2) show the height variation of granular volumetric concentration, average mixture horizontal speed, granular temperature, and granular shear viscosity taken at different positions and different times.

4.1. General Descriptions

4.1.1. Simulation PF_1 (Figures 11a−11b, Movie 5, and Figure 13a)

[41] After 30 s, the flow has reached a distance of 1.4 km with a well-developed head of 400 m high and with ε_s ranging from 9×10^{-5} vol.% at the base to $\sim 10^{-2}$ vol.% higher up (Figure 13a). The horizontal speed of the head is 9 m/s at the base and 34 m/s at a height of 20 m. The head has a well-developed overhang (nose) acting as a funnel for air (preferential entrainment). Consequently, the bottom of the head is much more diluted and slower than higher up. According to our classification scheme, this head has all the properties of a surge (predominately kinetic and mildly collisional). At 80 s, the head is 3.7 km away from source and has so much entrained fresh air that its concentration has decreased by a factor 10^3 (e.g., $\varepsilon_s \sim 10^{-5}$ vol.%). Such drop in concentration has drastically decreased the horizontal momentum (e.g., $U_x \sim 13$ m/s). At 100 s, the front of the flow is at a distance of 4.3 km with a basal collisional
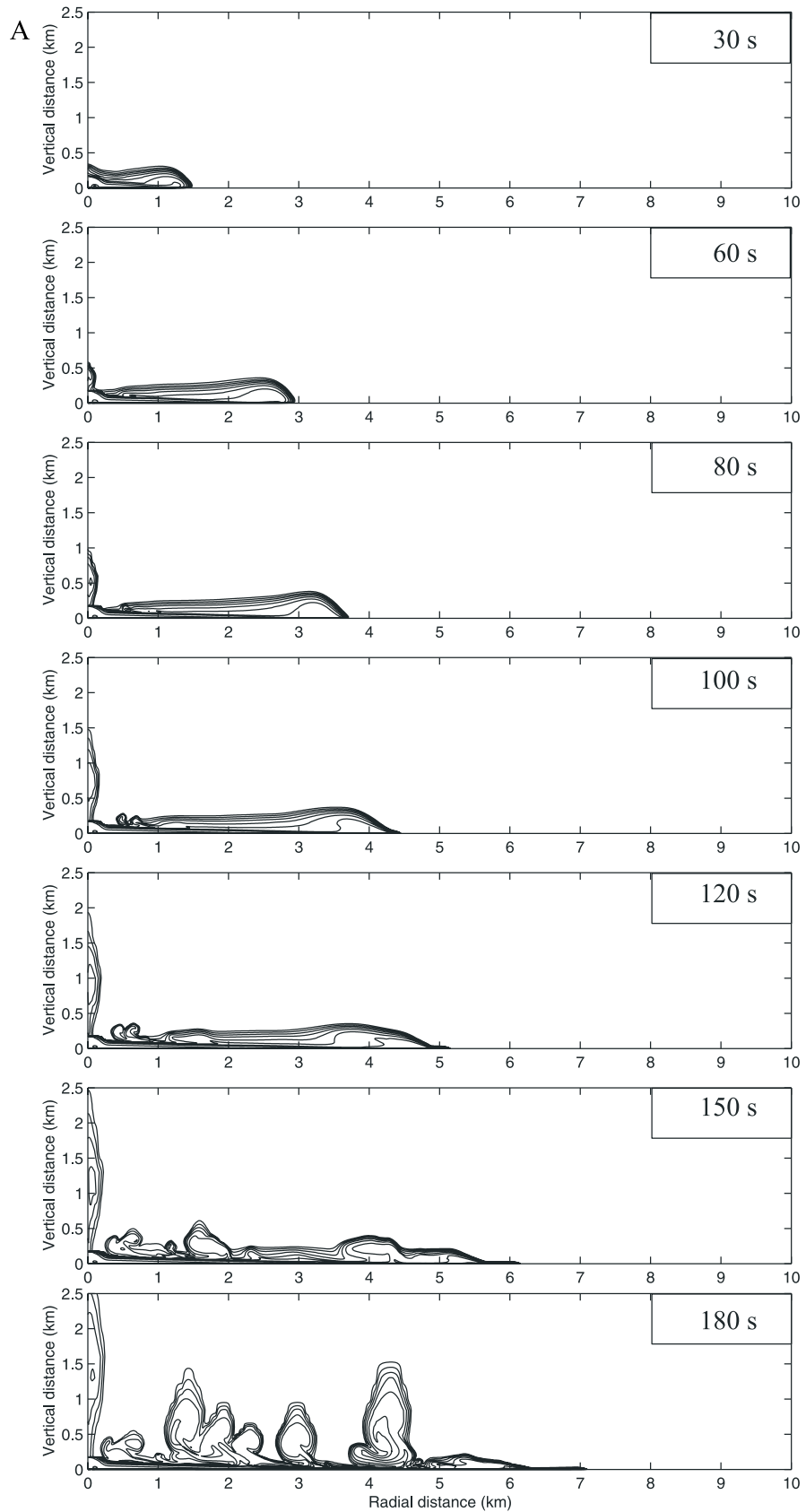
Figure 11

pyroclastic flow outrunning what remains of the dissipated head (see Figure 13a and Figures 11a–11b at 80s, 100s, 120s). The basal pyroclastic flow has a concentration of ~30 vol.% and travels at a maximum horizontal speed of ~45 m/s. Because this basal undercurrent lies in the purely collisional regime its granular temperature and granular shear-viscosity are very low ($\ll 10^{-4}$ m²/s² and $\sim 10^{-3}$ Pa·s, respectively; see Figure 13a) [*Dartevelle*, 2004]. The other striking feature is that within a height of 5 m the volumetric concentration decreases from 30 to 0.1 vol.%, suggesting a sharp concentration gradient between the basal PF and the overlying PS. In other words, there is no progressive transition between the basal dense PF (purely collisional regime) and the overlying diluted PS (kinetic regime). We will explain below how and where this basal concentrated flow is formed (section 4.2.1). At 180 s, the basal PF has outrun the rest of the flow and has traveled 7.2 km. Closer to source, phoenix clouds start to form because the flow system is losing its horizontal momentum which leads to sedimentation on the ground and dilutes the upper part of the flow which becomes positively buoyant [*Dobran et al.*, 1993]. At 240 s, the flow front is detached from the rest of the flow system, and being not fed anymore, it progressively becomes more and more dilute until it comes to rest at about 300 s and 8.8 km. Note the inward draughts at the base of the rising phoenix cloud (between 3.5 and 6 km) which produces a necking effect within the rising coignimbrite cloud [*Dobran et al.*, 1993] as seen for instance during coignimbrite ash cloud development in the 1991 Mt. Pinatubo eruption [*Woods and Wohletz*, 1991; *Sparks et al.*, 1997]. At 480 s, the system forms a granular deposit ($\varepsilon_s \sim$ 60 vol.%) between 3.6 and 5.4 km with a thickness as high as 12.5 m and a second minor deposit between 6.6 and 7 km with a thickness of about 7.5 m.

4.1.2. Simulation PF_2 (Figure 12, Movie 6, and Figure 14a)

[42] After 10 s, the head of the flow is well formed but more dilute, smaller, and slower than in PF_1: 80 m high, with concentration 2×10^{-5} vol.% at the base, and 10^{-3} vol.% at the nose level, traveling with horizontal speeds of 5 m/s at the base and 12 m/s at the nose level. This head will eventually be outrun by a denser basal pyroclastic flow but much quicker than PF_1: at 40 s, this basal under-flow has a concentration of 15 vol.% with a maximum horizontal speed of 39 m/s, and granular shear viscosity of 2×10^{-3} Pa·s. The shear viscosity has decreased relative to the head because collisions dissipate the granular temperature; from ~ 1 m²/s² at 30 s (PS) down to $\sim 10^{-3}$ m²/s² at 40 s (PF). This undercurrent will eventually travel to 8 km (300 s), then be detached from the main system and as it is progressively diluted, it will be halted by inward winds at 9 km. In the meantime, the system starts to develop a phoenix cloud at 1.5 km from the source (much closer than PF_1 owing to the lower initial momentum). Secondary minor phoenix clouds are developed at a distance of about 4.8 km at 210 s and at 6 km at 480 s. Note that those phoenix clouds are much less vigorous than in PF_1 and tend to bend inward and even slide backward, pushed by draughts (Movie 6). At 480 s, the system forms a granular deposit ($\varepsilon_s >$ 60 vol.%) between 3.5 and 4.7 km with thickness of up to 10 m.

[43] The simulation PF_2 produces the same kind of results as PF_1 but much earlier in the time sequence (deposit, basal PF outrunning the head of the flow, etc.), more concentrated, a slower (head, PF) with a deposit having a smaller extent. Owing to the lower horizontal momentum of the PF_2 basal undercurrent, it is detached from the flow system at a later time (300 versus 240 s).

4.2. Discussion

4.2.1. Proximal Deflation Zone and Flow Transformations (Lateral and Vertical)

[44] A denser (predominantly collisional PF) basal underflow systematically outran downstream the initially more diluted suspension current (purely kinetic PS). This is well documented in various eruptions, e.g., in Montserrat, Katmai, Mount Pinatubo, Lascar [*Druitt*, 1998; *Calder et al.*, 2000]. We speculate that the initial highly diluted

Figure 11. Time sequence over 8 min of simulation PF_1 (1.78×10^7 kg/s). (a) Time between 30 and 180 s. (b) Time between 210 and 480 s. The curves represent the logarithm of the volumetric solid concentration ($\log_{10}\varepsilon_s$) between −1 and −9 (the atmosphere has initially no grain). Size of the domain: 10 km (radial) × 2.5 km (height). The computational domain is initially much bigger, but beyond 10 km and 2.5 km the grid resolution is so poor that it has no practical interest to be shown. The poor grid resolution to higher altitudes explains why the coignimbrite (phoenix) clouds have such a vertical elongated shape.
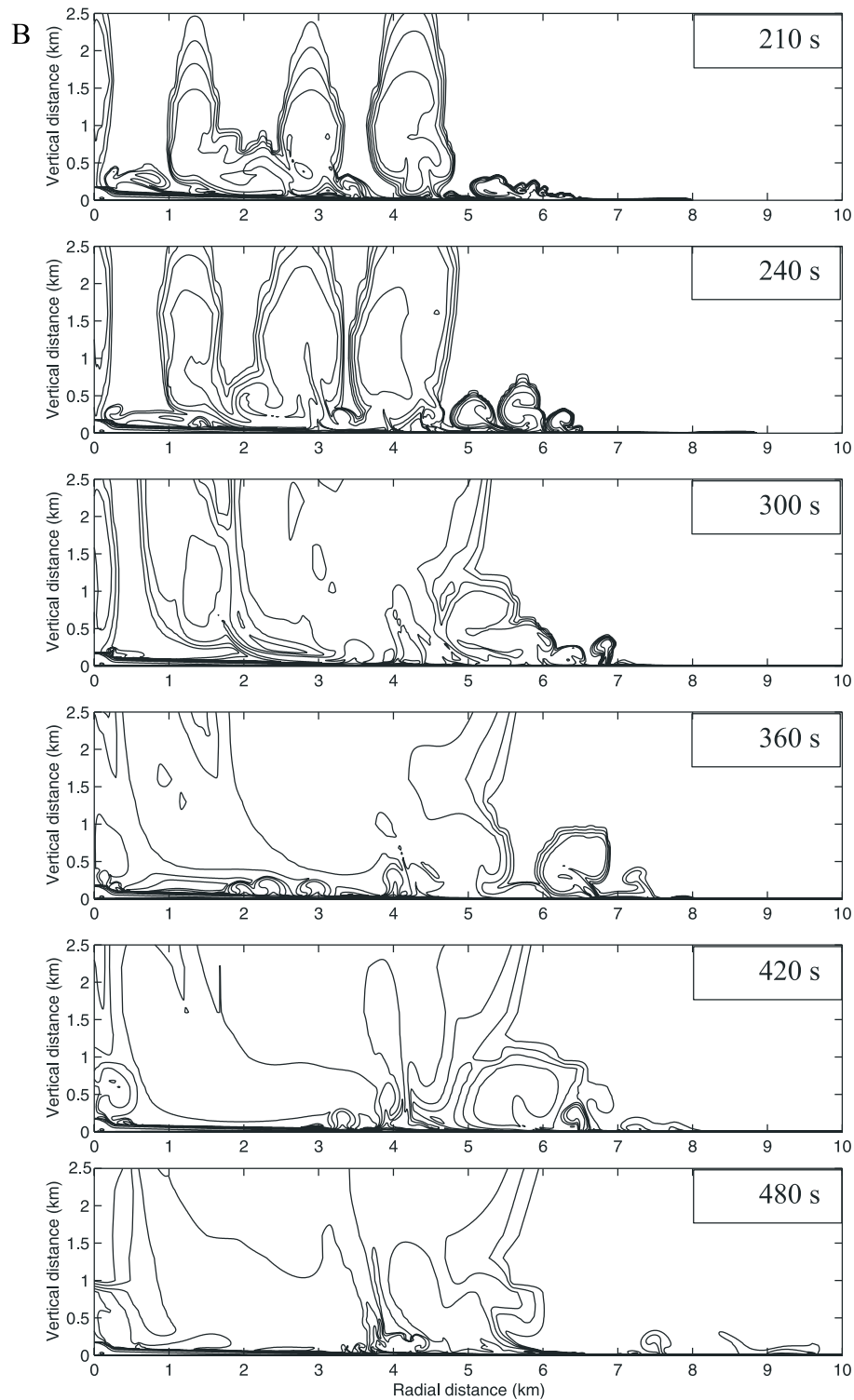
Figure 11. (continued)

head may deposit a thin layer, often named "ground layer," "ground surges," or "layer 1," found at the bottom of pyroclastic flow deposits (hence deposited first; see discussion by *Cas and Wright* [1988]). In our simulations, this ground-layer deposit cannot be modeled owing to the lack of vertical resolution. In the context of our simulations, the question is therefore where is this collisional undercurrent formed? *Sparks and Walker* [1977], *Sparks et al.* [1978], and *Walker*
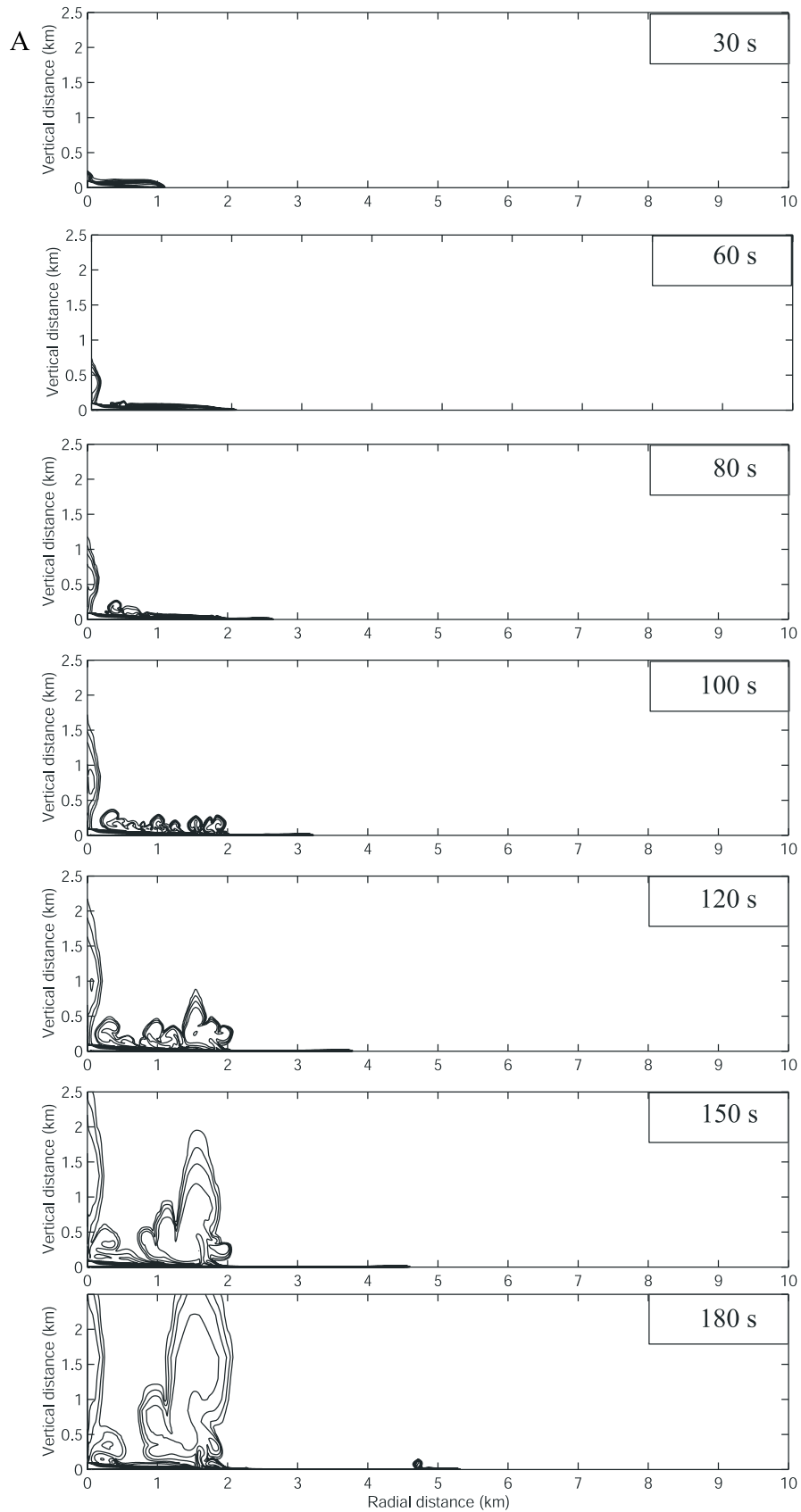
Figure 12

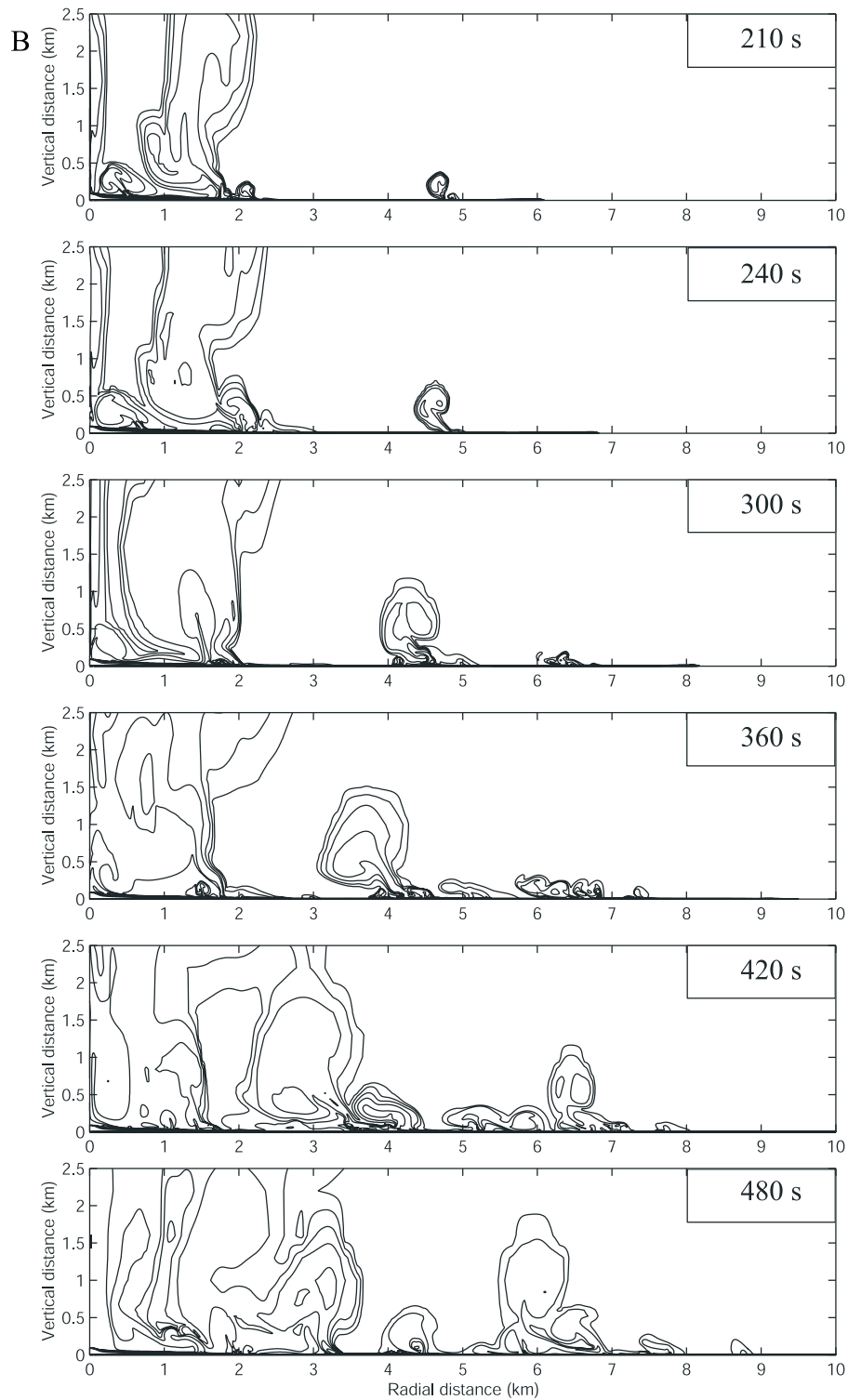**Figure 12.** (continued)

Figure 12. Time sequence over 8 min of simulation PF_2 (8.89×10^6 kg/s). (a) Time between 30 and 180 s. (b) Time between 210 and 480 s. Same volumetric concentration curves, domain size, and comments as in Figure 11.

A. Variable position and time sampling within the head of the flow:
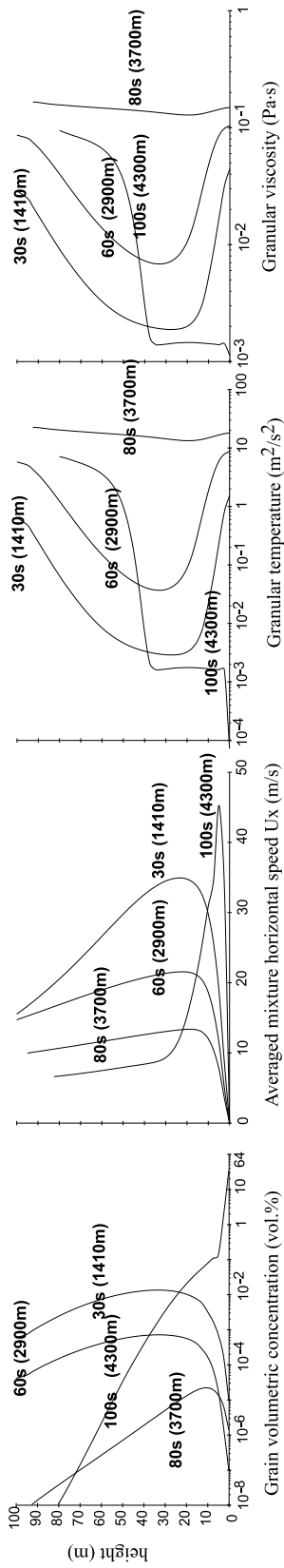
B. Fixed position sampling at 0.25 km from source:
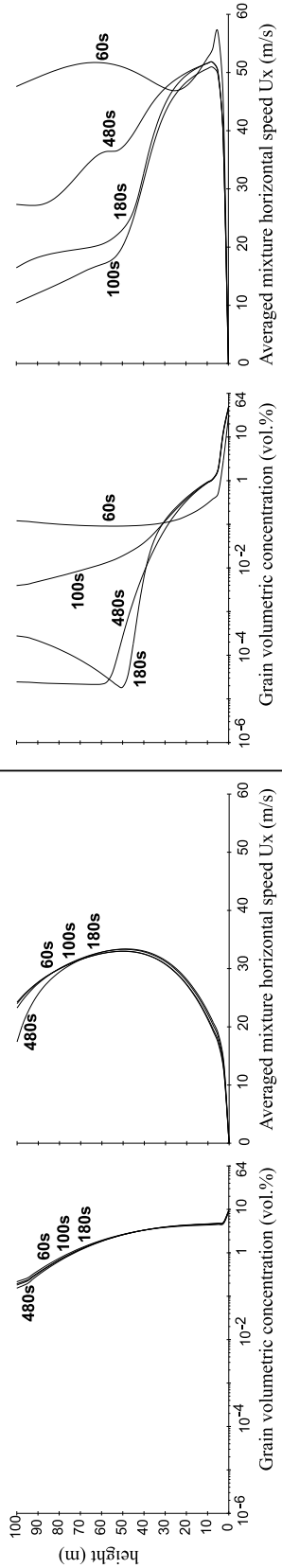
C. Fixed position sampling at 2.5 km from source:

D. Fixed position sampling at 4 km from source:

Figure 13

[1985] have suggested the existence of a "deflation zone" near the vent where denser pyroclastic flows are selectively segregating from a highly turbulent, diluted, expanded low-concentration flow (see a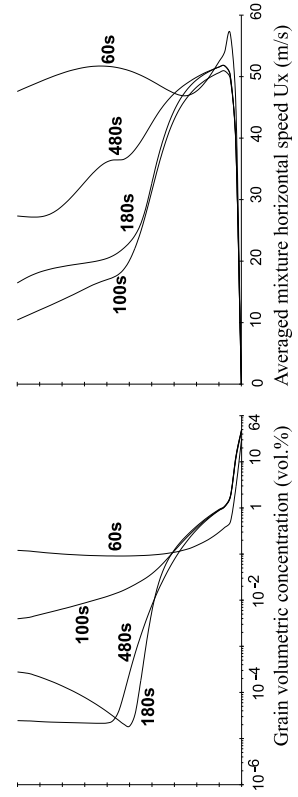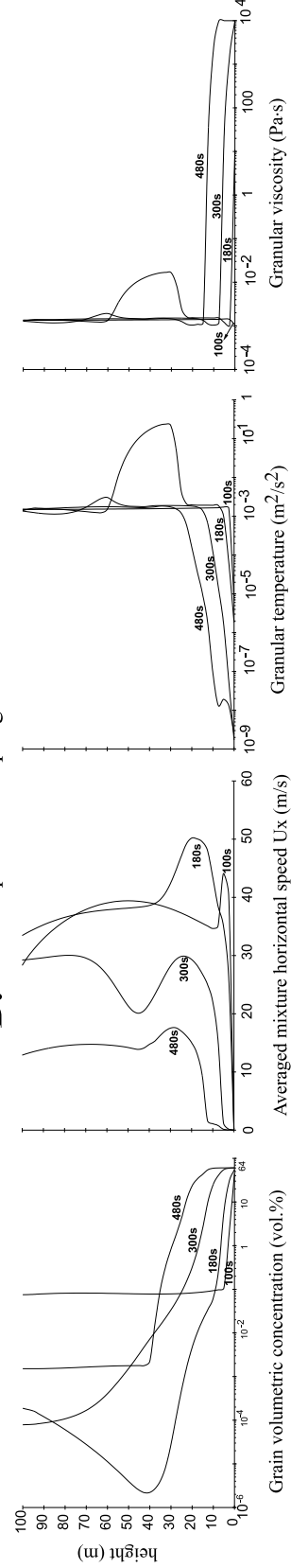lso the discussion by *Valentine and Wohletz* [1989]). Figure 13b (simulation PF_1) and Figure 14b (simulation PF_2) show ε_s and U_x within the flow sampled at different times 250 m from source, while Figure 13c and Figure 14c show the same variable sampling within the same time frame but 2.5 km from source. For both simulations, at 250 m from source, the concentrations (~0.1 to ~12 vol.%) and U_x (~13 to ~33 m/s) do not change significantly with time suggesting a self-maintained fluidized zone next to the vent. At 2.5 km, the situation is different as the concentration at the bottom of the flow increases with time (e.g., for PF_1 at 2.5 km: 32 vol.% at 60 s to ~50 vol.% at 480 s) and U_x values are much higher than at 250 m from source (i.e., for PF_1: between 40 to 58 m/s and for PF_2: 28 to 36 m/s). Hence, from this observation, we may conclude that the denser basal PF has been partially segregated from an upstream source.

[45] The second important feature is the relationship between the overlying PS and the basal PF. For instance, in Figure 13c, there is a sharp decrease of ε_s along the vertical direction within 5 m (at 480 s, from 50 vol.% at the base to less 0.1 vol.% at a height of 30 m) which shows the presence in this simulation of an active dilute suspension flow (a kinetic-collisional pyroclastic surge moving as fast as 50 m/s) over a basal underflow (predominantly collisional, slightly frictional moving at 40 m/s). This indicates that overlying dilute suspensions may also have an important role in the grain "feeding" of the basal PF. Yet, in simulation PF_2 (Figure 14c, Movie 6), there is no obvious overlying surge further downstream than 2 km, which would suggest, in this case, that the denser basal PF is solely laterally segregated from the proximal "deflation zone."

[46] The term "deflation" zone deserves to be clarified in this context. As previously noted by *Valentine and Wohletz* [1989], the concentrations in the "deflation" zone can be much higher than

further downstream. For instance, simulation PF_1 (Figures 13b and 13c), at 480 s, 40 m high, $\varepsilon_s \sim 5$ vol.% which is a predominantly a collisional regime (i.e., a maintained fluidized PF) and, at 2.5 km downstream, $\varepsilon_s \sim 10^{-2}$ vol.%, which is a kinetic-collisional regime (i.e., a dilute PS). Simulation PF_2 shows even sharper trends: at 480 s, 5 m high, at 250 m away from source, $\varepsilon_s \sim 3$ vol.% (Figure 14b) and, at 2.5 km from source, $\varepsilon_s \sim 10^{-3}$ vol.% (Figure 14c). Hence the deflation zone is not necessarily where the particle-laden flow is the most dilute. Nevertheless, it is certainly where basal concentrated pyroclastic flows start to laterally segregate. It also indicates that higher up in the flow, there is a lateral transformation from a fluidized, collisional PF (near source) to a much more diluted and kinetic PS further downstream. We would rather suggest renaming "deflation zone" to "maintained fluidized zone" as the former term would be synonym of "dilute" in the volcanological context.

4.2.2. Progressive Aggradation Versus en Masse Deposition

[47] For many decades volcanologists have debated whether pyroclastic flows and other geophysical granular gravity currents are deposited en masse (i.e., the flow suddenly and as a whole "freezes") or by progressive vertical aggradation (i.e., by a sustained sedimentation from a more diluted overlying current) [e.g., *Branney and Kokelaar*, 1992; *Druitt*, 1998; *Calder et al.*, 2000]. In the former case, the thickness of the flow unit and the parent flow are essentially the same, while in the latter, it implies a continuous sediment feeding from a more dilute current above the deposit. Any stratification within the aggradational deposit would reflect changes in flow steadiness, in the materials supplied at the source, or sedimentation time-break [*Branney and Kokelaar*, 1992; *Druitt*, 1998]. Since our model specifically links together granular shear viscosity, yield strength of the granular flow, and its concentration through the plastic potential and critical state theories [*Dartevelle*, 2004], our simulations may shed light on the exact nature of the depositional process.

Figure 13. Various time and space sampling along a height of 100 m within the flow PF_1. (a) Sampling at different positions and times within the head of the flow; from left to right: volumetric grain concentration (ε_s in vol.%), mean mixture horizontal speed (U_x in m/s), granular temperature (Θ in m^2/s^2), and granular shear viscosity (in Pa·s). (b) Sampling of ε_s and U_x at a fixed position 250 m from source at different time (60, 100, 180, 480 s). (c) Same sampling as in Figure 13b but at 2.5 km from source. (d) Sampling of ε_s, U_x, Θ, and granular shear viscosity at a fixed position 5 km from source for different times (100, 180, 300, 480 s).
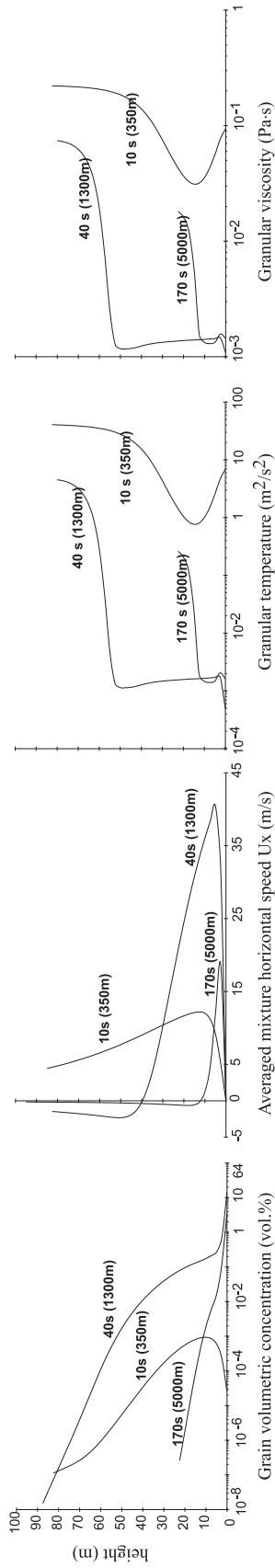
Figure 14

[48] Figure 13d (PF_1) and Figure 14d (PF_2) show at a fixed position (4 and 3.7 km, respectively) the volumetric grain concentration, averaged mixture horizontal speed, granular temperature, and granular shear viscosity of the flow sampled at different times. PF_1 has, at 100 s, a basal concentration of 44 vol.% and is flowing with a horizontal speed of ~40 m/s. This collisional pyroclastic flow has low granular temperature ($\sim 10^{-5}$ m^2/s^2) and low granular viscosity ($\sim 10^{-3}$ Pa·s). At 180 s, the flow shows plastic-frictional behavior ($\varepsilon_s \sim$ 55 vol.%) with U$_x$ at the base reduced to 26 m/s, and granular shear viscosity increased by a factor of ten thousand (~ 10 Pa·s). At 300 s, the basal part of the flow has reached a concentration of ~60 vol.% over a height of 7.5 meters and, at 480 s, over a height of 12.5 meters. At those concentrations, at the base of the flow, U$_x \sim$ 0 m/s, the granular temperature is negligible and shear granular viscosity is $\sim 10^4$ Pa·s (the maximum allowed in our model). Simulation PF_2 shows the same trends, however slower and more progressive, at a distance of 3.7 km: at the base, at 200 s, $\varepsilon_s \sim$ 51 vol.%; at 360 s, $\varepsilon_s \sim$ 58 vol.% (not shown on Figure 14d), and at 480 s, $\varepsilon_s \sim$ 60 vol.% over a height of 7.5 m (which is quasi-idle: U$_x \sim$ 0 m/s).

[49] From these figures, with time, the overall deposit is progressively building upward, which supports a progressive aggradation mechanism as the main depositional process. At any given location, the deposit as a whole is diachronous [*Druitt*, 1998]. The base is formed from sediments deposited much earlier from either above or from upstream locations. While, progressively upward in the deposit sequence, sediments are deposited from later and upstream parts of the flow. This is demonstrated by the progressive reduction of U$_x$ with time and at any given height within the flow and, also, by the reduction of U$_x$ from bottom to top (e.g., Figure 13d).

[50] It should be also mentioned that PF_1 and PF_2 have an important differences in the nature of the overlying surges: these are dilute and quasi nonexistent or PF_2 (Figure 14d), while active, fast, and moving further downstream for PF_1

(Figure 13d). Hence vertical aggradation and formation of a subsequent deposit are the result of two processes for PF_1: (1) sedimentation from the overlying surge and (2) supply of fresh granular materials by frictional flow coming from upstream. For PF_2, the major source of sediments is mainly from what is brought by frictional flow coming from upstream locations. In all the cases, these plastic-frictional flows are initially generated from the "maintained fluidized zone," near source, following this lateral flow transformation:

Collisional fluidized PF (near source) → kinetic PS
   → collisional PF → frictional PF → deposit.

[51] This implies that at any given height within the deposit sequence, an elementary flow unit stops when its yield strength becomes infinite, hence when its concentration is close to $^{max}\varepsilon_s \sim$ 64 vol.%. Therefore our mathematical model fundamentally generates a deposit by en masse freezing of an elementary flow unit when concentrations reaches ~64 vol.%. Each flow unit is built with fresh sediment brought either from upstream sources (lateral accumulation by plastic-frictional flows) or, if any, from overlying surges (vertical accumulation by sedimentation). Our model implies that en masse freezing is not at all antagonistic with vertical aggradation; the former acts on an elementary flow unit, the latter acts over the whole deposit sequence as seen on Figure 13d and Figure 14d. Our model and numerical results are consistent with field observations [e.g., *Calder et al.*, 2000] and naturally reconciles opposing views of depositional processes.

4.2.3. Pyroclastic Flow and Surge Relationships

[52] A close inspection of Figure 13 and Figure 14 demonstrates that both pyroclastic flows and surges have an intertwined history. As initial conditions, the flow was diluted at the source (see Table 1a) and eventually segregates into a denser basal pyroclastic flow and into a more dilute suspension above it. By sedimentation and by continuous feeding from upstream the bottom of the flow will eventually come to rest. In the previous section, we
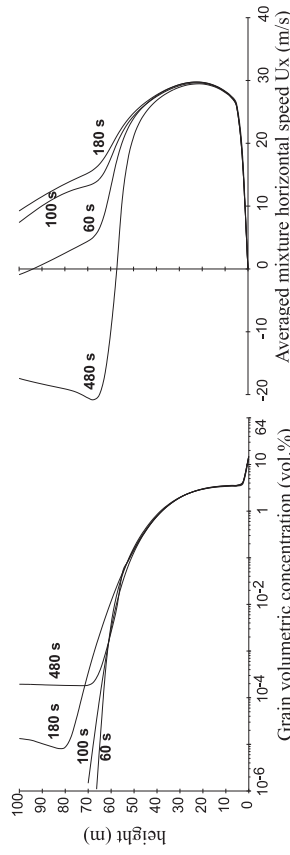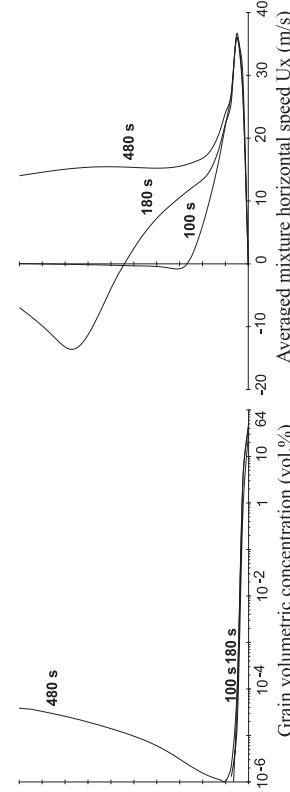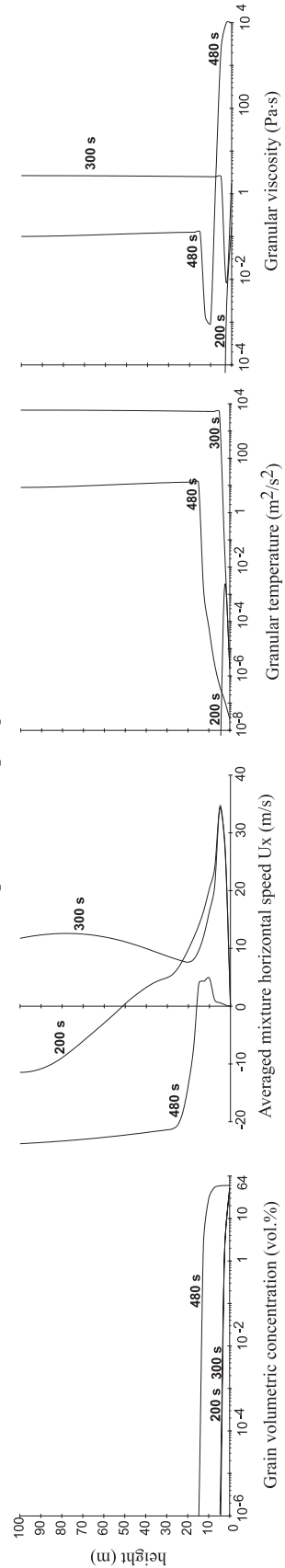
Figure 14. Various time and space sampling along a height of 100 m within the flow PF_2. (a) Sampling at different positions and times within the head of the flow; from left to right: volumetric grain concentration (ε_s in vol.%), mean mixture horizontal speed (U$_x$ in m/s), granular temperature (Θ in m^2/s^2), and granular shear viscosity (in Pa·s). (b) Sampling of ε_s and U$_x$ at a fixed position 250 m from source at different time (60, 100, 180, 480 s). (c) Same sampling as in Figure 14b but at 2.5 km from source for time 100, 180, and 480 s. (d) Sampling of ε_s, U$_x$, Θ, and granular shear viscosity at a fixed position 3.7 km from source for different times (200, 300, 480 s).

Inviscid Flow Model
PF_3

Kinetic-Collisional-Frictional Flow Model
PF_1

A. Volumetric grain concentration sampled at 5.2 km from source

important deposition: 5m of thickness increase within 3 minutes

no deposition, no thickness variation with time
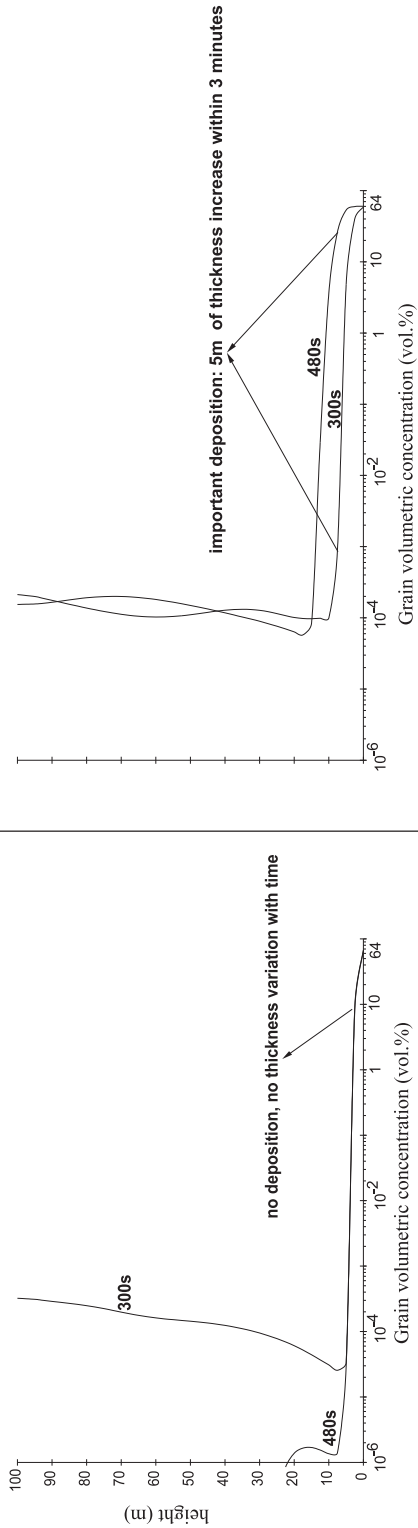
B. Averaged mixture horizontal speed sampled at 5.2 km from source

important horizontal speed decrease
(from 26 to 0 m/s at an height of 2.5 m)
within 3 minutes as depsotion occurs

no horizontal speed variation
with time

Figure 15

have seen a lateral flow transformation occurs from PF close to source into PS further downstream. In addition, by sedimentation, the overriding PS current looses its momentum and becomes sufficiently dilute to loft and form phoenix clouds as seen in Figure 11 (e.g., 180 s) and Figure 12 (e.g., 100 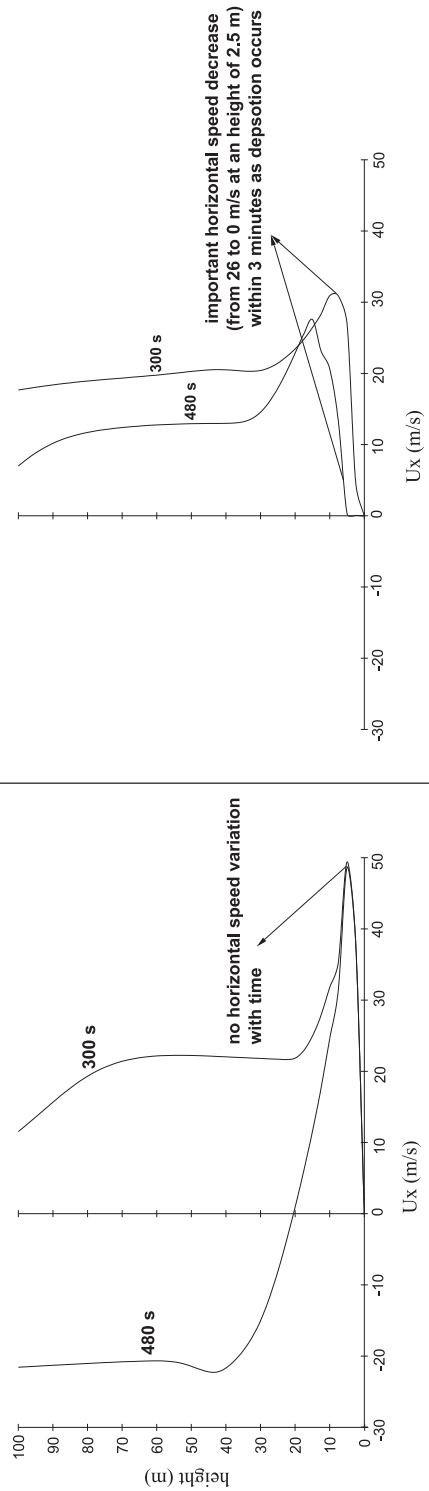s). These coignimbrite clouds may afterward feed the system with new fallouts as they are pushed back and forth by inward and outward draughts.

[53] From Figure 13 and Figure 14, any properties of the flow (concentration, velocities, so forth) sharply change with time (unsteadiness) and space (nonuniformity, both vertically and horizontally) [*Freundt and Bursik*, 1998]. Globally, it is difficult to see the whole pyroclastic phenomenon with only one of the end-members (i.e., either dilute or concentrated), which justifies a multiphase model approach, able to model the whole spectrum of volumetric grain concentrations provided that a comprehensive rheological model is implemented in the code (see section 4.2.4).

4.2.4. Viscous Versus Inviscid Flow

[54] As mentioned in the companion paper [*Dartevelle*, 2004], a vast array of granular viscosities have been measured in chemical engineering, fluid dynamics, and volcanology. For instance, after the 1980 eruptions of Mt. St. Helens, *Wilson and Head* [1981] measured, in the newly deposited pyroclastic flows, viscosities in the range $O(10)$ to $O(10^4)$ Pa·s from which they rightly suggested that concentrated pyroclastic flows may behave plastically. It is worth noting that in our simulations when the pyroclastic flows reaches a volumetric grain concentration of 60 vol.%, our calculated granular shear viscosities are in the same range as those measured by *Wilson and Head* [1981] (e.g., see Figure 13, Figure 14, and also Figure 4 of *Dartevelle* [2004]). However, to date, most current models of pyroclastic flows and surges assume either empirical low-viscosity linear rheologies (e.g., Newtonian, Bingham) or no viscosity at all.

[55] To compare our model with an inviscid model, we have computed simulation PF_1 assuming that there is no kinetic-collisional-plastic behavior and setting the granular shear and bulk viscosities and

the granular plastic pressure to zero. However, it is still necessary to use the normal component of the solid stress to prevent the particles from reaching impossible high values [e.g., *Bouillard et al.*, 1991; *Gidaspow*, 1994; *Neri and Macedonio*, 1996; *Todesco et al.*, 2002]. Since we have now turned off the plastic formulation of ^fP [*Dartevelle*, 2004, equation (T5.19)], we will use the same empirical formulation as in PDAC2D codes to roughly estimate the solid pressure [e.g., *Neri and Macedonio*, 1996; *Todesco et al.*, 2002]:

$$\nabla P_s \approx G(\varepsilon_s)\,\nabla\varepsilon_s = 10^{-3.33+8.76\varepsilon_s}\,\nabla\varepsilon_s, \qquad (3)$$

where the "compressibility modulus," $G(\varepsilon_s)$ in Pa, is an empirical best fit (among many others) of chemical engineering fluidization data [*Bouillard et al.*, 1991]. $G(\varepsilon_s)$ is sometimes named "elastic modulus" and the whole expression given by equation (3) is named "Coulombic component" [e.g., *Neri and Macedonio*, 1996; *Todesco et al.*, 2002], which is a misleading terminology because $G(\varepsilon_s)$ is only empirical and not related to any elastoplastic theoretical model. With this in mind, it is easy to implement ∇P_s given by equation (3) into the momentum equations of the solid phase [*Dartevelle*, 2004, equation (T1.6)].

[56] Figure 15 shows the solid volumetric concentration and averaged mixture horizontal speed versus the height at a location of 5.2 km from source for time 300 and 480 s. The full rheological model (right side of Figure 15) shows a vertical aggradation (~64 vol.% over a height of 5 m) and a sharp decrease of U_x to nil value (i.e., deposit). The inviscid model (left side of Figure 15) shows no deposition and no vertical aggradation at all. Even though ε_s is as high as 66 vol.% on the ground with the inviscid model, the horizontal speed is still as high as 40 m/s, which is physically questionable for such a high concentration. Note also the very different velocity and concentration profiles higher up in the dilute part of the flow. The inviscid model makes the dilute part of the flow strongly sensitive to inward draughts, i.e., surges and coignimbrite flows cannot move on their own as they cannot offer any rate-of-strain "resistance" imposed by draughts, hence they "fly" along the

Figure 15. Comparison of numerical results from a fully inviscid model (left side) and a full rheological granular model (right side) involving kinetic-collisional and plastic formulations as in *Dartevelle* [2004]. Sampling at a fixed distance of 5.2 km from source at two different times (300 and 480 s). (a) Volumetric grain concentration versus height in the flow. (b) Averaged mixture horizontal speed versus height. The inviscid model is unable to build up a deposit (no vertical aggradation) and to stop; i.e., the horizontal speed is higher than 40 m/s for concentrations as high as 66 vol.%.

main draught directions. The runout distance of the flow is only imposed by the severity of the counter-drafts.

5. Conclusions

[57] Within the assumptions of our physical models (e.g., 2-D simulation, one grain size, no water phase change, no coupling between turbulence in the gas and dispersed solid phase, see *Dartevelle* [2004]), we have performed plinian cloud, pyroclastic surge and flow simulations in order to validate and compare our numerical results with remote-sensing data, historical eruptions, classical plume theories and field observations and, also, to shed new light on some of the most debated issues in volcanology about the nature and dynamic of pyroclastic flows.

[58] Our plinian column simulations correlate well with *Morton et al.* [1956] plume theory and historical eruptions in the top altitude of the cloud (H_T) versus mass flux diagram. The high mass flux eruption columns ($>10^7$ kg/s) are highly nonlinear, chaotic and subject to quasiperiodic vertical acoustic-gravity waves generated at the transition jet-plume area. H_T fluctuates with time over 1 hour; hence temperature anomalies at "the tip of the top" of the cloud range between -11 K and $+20$ K. These results compare well with Mt. Pinatubo, El Chichón and Mt. St. Helens eruptions. The largest plinian simulation shows the development of important convective supercell in phase with the vertical propagation of acoustic-gravity waves. The plinian simulations show complex, unsteady, and heterogeneous velocity and solid volumetric concentration profiles within the clouds (in the column and in the umbrella). To our the best of our knowledge, to date, (G)MFIX is the first multiphase model able to simulate complete stable plinian clouds.

[59] The pyroclastic flow and surge simulations display nonlinear and highly viscous behaviors. Our simulations show complex lateral flow transformation processes (pyroclastic surges↔pyroclastic flows). The head of the flow is diluted and has all the properties of a pyroclastic surge, which is eventually outrun by a collisional, denser basal undercurrent pyroclastic flow. Our simulations suggest that the depositional process is mostly gradual with materials supplied either by downstream currents or/and by sedimentation from overlying surges. However, it is shown that gradual deposition is not incompatible with en masse deposition. The subsequent deposit is diachronous from base to top. Deposition does not occur uniformly everywhere, e.g., our simulations show the presence of "maintained fluidized zone" near source.

[60] In the long run, our multiphase simulations suggest that the Large Eddy Simulation (LES) should be the ideal mathematical and physical framework to further develop multiphase turbulence models in accounting for the coupling between phasic turbulence effects and for mass transfers between phases (e.g., Sub-Grid Mass flux for water phase change).

Appendix A: Grid Size Analysis for Geophysical Flows

[61] Although previous studies have shown that MFIX codes produce results independent on the grid size [*Guenther and Syamlal*, 2001], this must be also demonstrate for geophysical applications (plinian cloud and pyroclastic flow and surge simulations). This is important to establish owing the relative poor resolution of all our simulations and the simplifications in our model [*Dartevelle*, 2004]. Of course, a highly coarse grid size may produce unrealistic physics, may prevent from obtaining a solution (no convergence), and/or may prevent from forming a granular deposit at the ground level in the pyroclastic flow simulations. In addition, the values of any seemingly realistic solutions can only be valued if grid size independence is somehow demonstrated within the typical range of grid size used in this project.

[62] Table A1 presents two identical plinian simulations achieved with different grid sizes: a grid size of 50 m over the whole height and over a radial distance of 6.2 km and a grid size of 100 m over the whole height and over a radial distance of 7 km. Figure A1 shows the results over one hour for both simulations. Clearly no significant differences can be seen even if as expected more details in the eddy structures and the umbrella shape (multilayered, thickness) appeared between both simulations. However, both radial distance and top altitude are essentially the same. Since the plinian column simulations have been achieved with a grid size much smaller than 100 m (i.e., 30 m for PL_1, 50 m for PL_2, 80 m for PL_3), we may conclude that the numerical results produced in this manuscript are grid size independent.

[63] Table A2 presents four identical simulations of pyroclastic flows and surges achieved with differ-

Table A1. Grid Size Analysis for Plinian Cloud Simulations: Initial and Boundary Conditions

Eruption	Grid 50 m	Grid 100 m
Geometry	Cylindrical	Cylindrical
Vertical length Y, km	30	30
Vertical resolution ΔY, m	50	100
Number of grid point in the Y direction	601	301
Radial length X, km	30	30
Radial resolution from 0 to 6.2 km ΔX, m	50	100
Radial resolution from 6.2 to 7.0 km ΔX, m	100	100
Radial resolution from 7.0 to 7.4 km ΔX, m	200	200
Radial resolution from 7.4 to 8.2 km ΔX, m	400	400
Radial resolution from 8.2 to 9.0 km ΔX, m	800	800
Radial resolution from 9.0 to 30.0 km ΔX, m	1000	1000
Number of grid point in the X direction	158	96
Vent diameter, m	200	200
Mixture vertical speed V_y, m/s	80	80
Volumetric solid concentration ε_s, vol.%	0.1	0.1
Grain diameter d, μm	50	50
Grain microscopic density ρ_s, kg/m^3	1500	1500
Mixture temperature at the vent T_m, K	900	900
Gas pressure at the vent P_g, Pa	10^5	10^5
Mass fraction of water vapor at the vent	1.0	1.0
Calculated mixture density ρ_m, kg/m^3	1.74	1.74
Calculated mass flux, kg/s	1.75×10^7	1.75×10^7

ent grid size at the ground. One run has a very high vertical resolution at the ground level (1.25 m), the others have a coarser vertical resolution by a factor two: 2.5, 5.0, 10 meters. The results of these four simulations are shown in Figure A2 at two different times (40 and 100 s) and in Figure A3, where we compare the solid volumetric concentration (ε_s) and the averaged horizontal speed (Ux) at 40 s and 100 s. In Figure A2, there is no difference on the global scale: all produce at the same distance from source the same coignimbrite ash cloud. However, the coarser the grid size at the ground level, the more delayed the formation of the deposit (for the 10 m grid size run, it has not yet happened) as seen on Figure A3. There is no significant difference for the 1.25, 2.5 and 5.0 m in the formation of a concentrated deposit at the bottom. The only difference is that the deposit is developed very early in the time sequence with the high resolution grid, 1.25 m (therefore being well-frozen after 100 s), while just barely formed after 100 s with the 5.0 m grid (and not yet quite frozen). The grid resolution of 10 m seems not to be adequate because deposition only occurs over on height of 12 m, which cannot be capture with a grid size of similar scale. In all the cases, it can be seen that there is a sharp deceleration between 40 s and 100 s due to the grain deposition and the plastic rheological model of *Dartevelle* [2004]. In conclusion, Figures A2 and A3 suggest that the choice we have made for a 2.5 m grid size at the ground for simulation PF_1 and PF_2 is fully adequate to

capture the main features of sedimentation processes. A higher resolution at the ground would only be possible with much more powerful computer capabilities. These results are fully consistent with *Dobran et al.* [1993] and *Neri et al.* [2003].

Appendix B: Overview of the Numerical Schemes Used in MFIX and (G)MFIX

[64] In a typical multiphase system, the momentum and energy equations (and also mass if phase transition occurs) are highly coupled through exchange terms. Those exchange terms strongly couple the components of velocity, temperature (and possibly mass) in a given phase to the corresponding variable in the other phase. This property is called the "interequation coupling." In addition, the discretized equations are nonlinear because the coefficients of the discretized equation depend on the values of the variable to be found. (G)MFIX uses a semi-implicit numerical scheme which must specifically deal with the interequation coupling and the nonlinearity of the discretized equations. To linearize the equations, the iterative method of Newton could be used [*Press et al.*, 1986] but it is more economical and practical, particularly for the momentum equations, to use the Patankar and Spalding's SIMPLE algorithm (Semi-implicit for Pressure Linked Equations) [*Patankar*, 1980; *Spalding*, 1981, 1983; *Patankar et al.*, 1998; *O'Rourke et al.*, 1998; *Syamlal*, 1998;
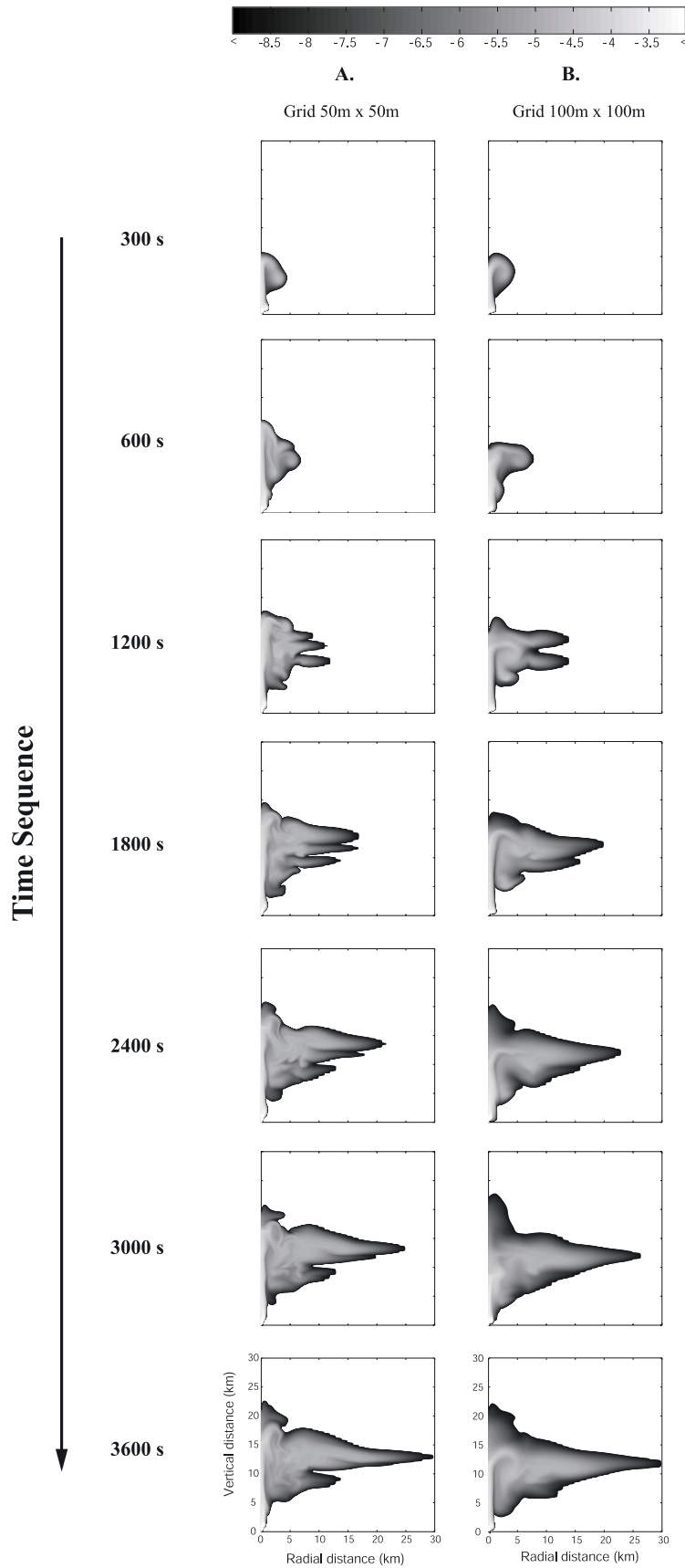
Figure A1

Table A2. Grid Size Analysis for Pyroclastic Flow Simulations: Initial and Boundary Conditions

Eruption	Grid 1.25 m	Grid 2.5 m	Grid 5.0 m	Grid 10 m
Geometry	Cartesian	Cartesian	Cartesian	Cartesian
Vertical length Y, km	10	10	10	10
Vertical resolution from 0 to 50 m ΔY, m	1.25	2.5	5.0	10.0
Vertical resolution from 50 to 100 m ΔY, m	2.5	2.5	5.0	10.0
Vertical resolution from 100 to 150 m ΔY, m	5.0	5.0	5.0	10.0
Vertical resolution from 150 to 400 m ΔY, m	10.0	10.0	10.0	10.0
Vertical resolution from 400 to 1000 m ΔY, m	20,40,80,160	20,40,80,160	20,40,80,160	20,40,80,160
Vertical resolution from 1 km to 10 km ΔY, m	300,600,1000	300,600,1000	300,600,1000	300,600,1000
Number of grid point in the Y direction	115	95	75	60
Radial length X, km	16	16	16	16
Radial resolution from 0 to 5 km ΔX, m	500	500	500	500
Radial resolution from 5 to 8 km ΔX, m	20,40,80,160	20,40,80,160	20,40,80,160	20,40,80,160
Radial resolution from 5 to 8 km ΔX, m	400,800,4800	400,800,4800	400,800,4800	400,800,4800
Number of grid point in the X direction	550	550	550	550
Vent diameter, m	50	50	50	50
Mixture vertical speed V_y, m/s	50	50	50	50
Volumetric solid concentration ε_s, vol.%	5.0	5.0	5.0	5.0
Grain diameter d, μm	250	250	250	250
Grain microscopic density ρ_s, kg/m³	2500	2500	2500	2500
Mixture temperature at the vent T_m, K	900	900	900	900
Gas pressure at the vent P_g, Pa	10^5	10^5	10^5	10^5
Mass fraction of water vapor at the vent	1.0	1.0	1.0	1.0
Calculated mixture density ρ_m, kg/m³	296	296	296	296
Calculated mass flux, kg/s	1.48×10^8	1.48×10^8	1.48×10^8	1.48×10^8

Pannala et al., 2003]. In the SIMPLE algorithm (Table B1), a system of coupled implicit equations is solved by associating with each equation an independent solution variable and solving implicitly for the value of the associated solution variable that satisfies the equation, while keeping the other solution variables fixed. For instance, pressure appears in all the momentum equations of all the phases (gas pressure in the gas momentum equations and solid pressure in the solid momentum equations), therefore making the velocity components dependent on the pressure value and vice versa (hence making the momentum equations nonlinear). Therefore, in the gas momentum equations, the pressure is chosen as independent variable and special treatment is used for solving the gas pressure (i.e., the pressure correction equation of *Patankar* [1980]; see also *Spalding* [1983], *Patankar et al.* [1998], and *Syamlal* [1998]). In the solid momentum equation, the solid volume fraction is chosen as an independent variable (i.e., the solid volume fraction correction equation)

[*Syamlal*, 1998]. To help convergence during the SIMPLE iteration process, an underrelaxation technique is used to slow down the changes in the coefficient from iteration to iteration with an underrelaxation factor, ω, less than unity [*Patankar et al.*, 1998] (see Table B1). The interequation coupling must be dealt with some degree of implicitness to ensure fast convergence in anticipating the effects of a change in the local property of one phase on the properties of the other phase at the same location and simultaneously [*Spalding*, 1981]. This is accomplished with the Partial Elimination Algorithm (PEA) of *Spalding* [1981] [see also *Syamlal*, 1998]. With PEA, in a given phase, all the coefficients of the discretized equations involving the exchange terms (e.g., momentum exchange, K, and heat transfer, Q, between phases; [see *Dartevelle* [2004, equation (T1.5) to equation (T1.8)]]) and the value of the corresponding variable from the other phase (e.g., velocities and temperature) are treated as source terms evaluated from the previous time step iteration [*Syamlal*, 1998]. Once both linea-

Figure A1. Time sequence over one hour of two plinian clouds. (a) The vertical grid size is 50 m and the radial grid size is 50 m over a distance of 6.2 km. (b) Same plinian cloud simulation but within a coarser grid size 100 m vertical and 100 m radial (over a distance of 7 km). Although many more details are captured with a high-resolution grid, the behavior and shape of the plinian clouds are essentially identical.
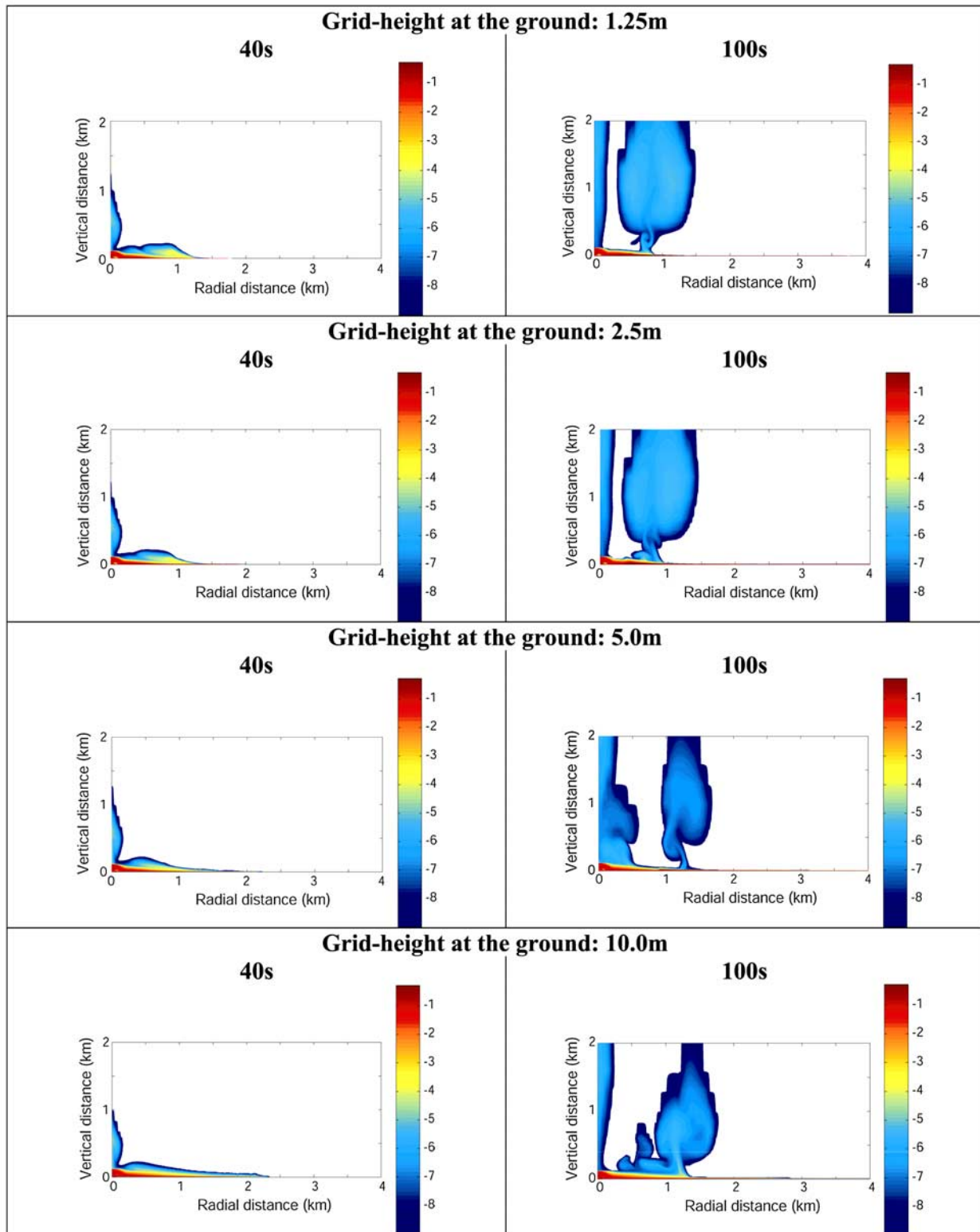
Figure A2. Snapshots taken at 40 s and 100 s of the same pyroclastic flow simulation but with different vertical grid size at the ground level: 1.25 m, 2.5 m, 5 m, and 10 m over a height of 50 m. It is worth noting that after 100 s in all cases, a phoenix cloud loft at a distance of 0.8 km and 1.2 km. With a coarser grid height both the formation of a deposit and of a phoenix cloud are somehow delayed in both time and space. A grid as coarse as 10 m does not seem appropriate to fully capture the sedimentation process within this time span.
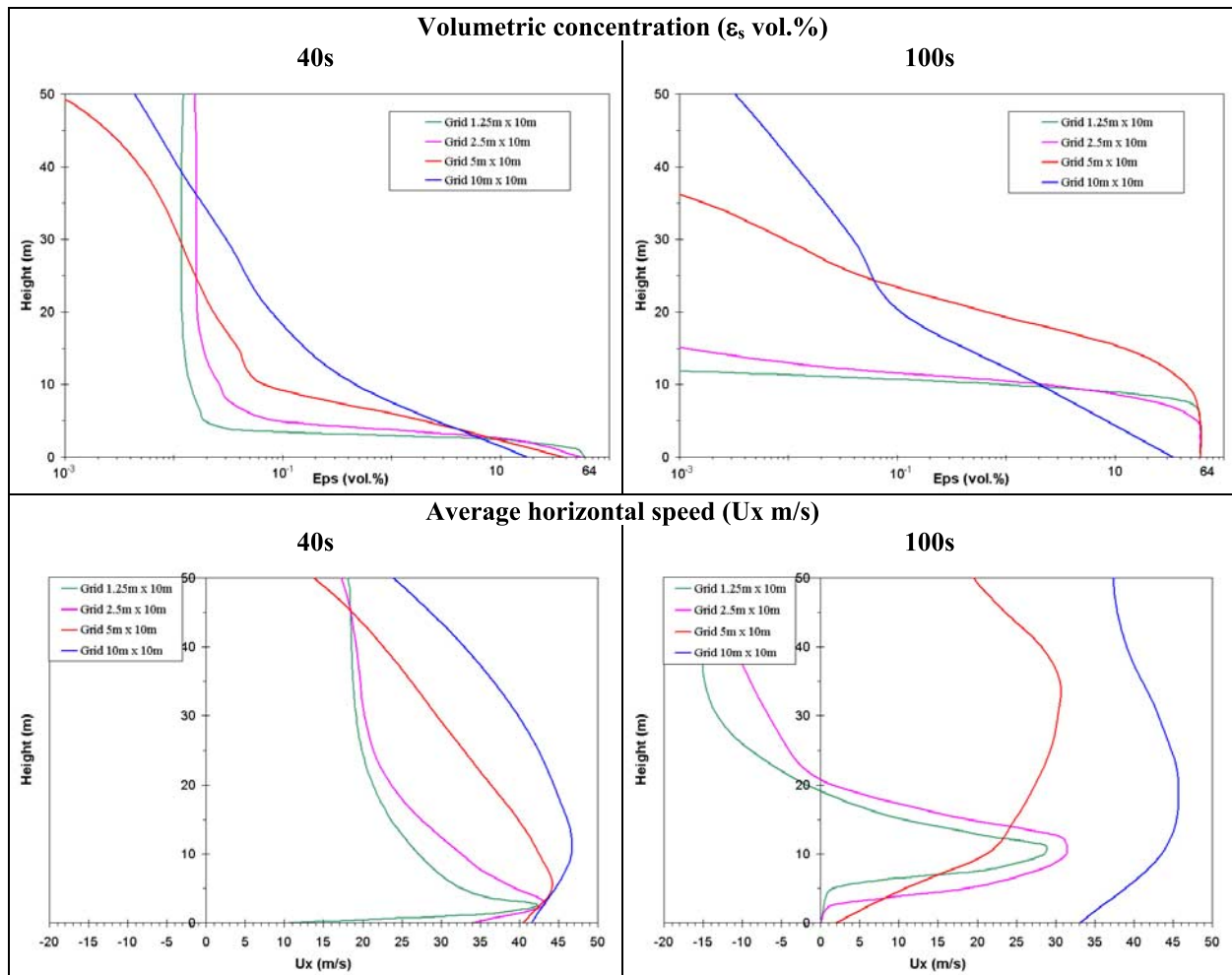
Figure A3. Grain volumetric concentration (ε_s in vol.%) and horizontal mixture speed (U_x in m/s) over a height of 100 m. After 100 s, a deposit is building up for all the grid heights except 10 m. This is also shown in the horizontal speed figures, where $U_x \sim 0$ m/s for the 1.25 m and 5 m grid and $\sim$2 m/s for the 5 m grid. The flow has barely decelerated within the 10 m grid. These figures suggest that the coarser the grid, the more delayed the sedimentation process. The typical grid size used in this manuscript (2.5 m) is largely sufficient to capture the sedimentation and depositional process and, more importantly, this 2.5 m grid size display results grid size independent.

rization and interequation are dealt, within the SIMPLE algorithm, (G)MFIX can solve the discretized equation using a classical linear solver iterative method (a point iteration, also called relaxation), such as the generalized minimal residual method (GMRES) [*Saad and Schultz*, 1986], and a more stable variant of the biorthogonal-conjugate gradient method (BI-CGSTAB of *van der Vorst* [1992]). See Table B1 for the specific linear solver/variable combination used in our simulations.

[65] (G)MFIX uses an automatic time step adjustment to reduce the total run time in achieving the best ratio of "time step"/"number of iteration needed for convergence" and this at any given simulation time [*Syamlal*, 1998]. For instance,

the semi-implicit algorithm imposes a very small time step for very dense gas-solid flow simulations or whenever sharp gradient develops within the flow field. On the other hand for quasi-steady diluted flows, a small time step would make the run unnecessarily long. MFIX monitors the total number of iterations needed for convergence for several previous time steps. If there is a favorable reduction in the number of iterations per second of simulation, then a small upward time step adjustment is performed. Or, for instance, if the simulation fails to converge for a given time step, then the time step is decreased till convergence is obtained [*Syamlal*, 1998]. Convergence of iterations in the linear equation solvers is judged from the residuals of various equations

Table B1. "SIMPLE" Algorithm for Multiphase Granular Flows in MFIX and (G)MFIX Codes[a]

Step	Procedure
1	Start of a new time step iteration. Calculate physical properties and exchange coefficients.
2	Calculate guessed velocity fields of both solid and gas phase ($^{\circ}\mathbf{u}_s$ and $^{\circ}\mathbf{u}_g$) on the basis of the available current pressure fields ($^{\circ}P_s$ and $^{\circ}P_g$) and volumetric concentrations ($^{\circ}\varepsilon_s$ and $^{\circ}\varepsilon_g$). Use BI-CGSTAB and PEA.
3	Calculate the gas pressure correction with BI-CGSTAB: $^{..}P_g$.
4	Update the gas pressure field with underrelaxation technique: $P_g = {}^{\circ}P_g + \varpi_g {}^{..}P_g$, where the underrelaxation factor for the gas phase: $0 < \varpi_g < 1$.
5	Calculate gas velocity correction fields ($^{..}\mathbf{u}_g$) from $^{..}P_g$ and update velocity fields: $\mathbf{u}_g = {}^{\circ}\mathbf{u}_g + {}^{..}\mathbf{u}_g$.
6	Calculate tentative estimates of solid velocity field knowing the updated $\mathbf{u}_g$ and P_g values: $^{1}\mathbf{u}_s$.
7	Calculate the solid volumetric concentration correction with BI-CGSTAB: $^{..}\varepsilon_s$.
8	Calculate solid velocity correction fields ($^{..}\mathbf{u}_s$) and update velocity fields: $\mathbf{u}_s = {}^{1}\mathbf{u}_s + {}^{..}\mathbf{u}_s$.
9	Update the solid volumetric concentration: $\varepsilon_s = {}^{\circ}\varepsilon_s + \varpi_s {}^{..}\varepsilon_s$, where the underrelaxation factor for the solid phase: • if $^{..}\varepsilon_s > 0$ (i.e., solid volumetric faction is increasing) and $\varepsilon_s > {}^{f}\varepsilon_s$ (i.e., where the contact between particle is frictional), then $0 < \varpi_s < 1$. • otherwise, $\varpi_s = 1$.
10	Update the gas volumetric concentration: $\varepsilon_g = 1 - \varepsilon_s$.
11	Update the solid pressure field P_s from ε_s.
12	Calculate solid and gas temperatures with BI-CGSTAB and PEA.
13	Calculate the granular temperature (if needed) with BI-CGSTAB.
14	Check for convergence judged from the normalized residuals of the linear equation solvers used in steps 2, 3, 7, 12, and 13: • If reached, start the next time step (step 1) and automatically adjust the time step. • If not reached, restart the iteration process (step 2) with the new corrected velocity fields, pressure fields, and concentration values.

[a] Multiphase SIMPLE algorithm in relation with Partial Elimination Algorithm and linear solver techniques used in the (G)MFIX codes. For the calculation techniques of pressure correction equation, solid volumetric correction equation, velocity field correction equations, underrelaxation factors, and Partial Elimination Algorithm (PEA) see *Patankar* [1980], *Spalding* [1983], *Syamlal* [1998], and *Patankar et al.* [1998]. For the linear equation solver techniques, such as the biorthogonal-conjugate gradient stable method (BI-CGSTAB), see *van der Vorst* [1992]. All symbols are defined in Appendix A of the companion paper [*Dartevelle*, 2004]. The physical properties and exchange coefficient are given in Tables 3 and 4 and Table 2, respectively, of *Dartevelle* [2004]. Typically, between 5 and 20 iterations are needed before declaring convergence. Note that at convergence the gas pressure ($^{..}P_g$) and solid volume fraction ($^{..}\varepsilon_s$) corrections must go to zero [*Syamlal*, 1998].

over the whole computational domain. Convergence is declared whenever each residual of each discretized equation within the same iteration tends to zero. If the residuals are not reduced, a supplementary iteration will be performed. If convergence is not obtained within a specified number of iterations (30 in our simulations), or if the system is divergent, then "nonconvergence" is declared and the time step is decreased.

[66] (G)MFIX uses portable OPEN-MP (for shared memory multiprocessors) and MPI (for distributed memory parallel computers) in a unified source code. The MFIX codes has been ported to a Beowulf Linux cluster, SGI SMP, Compaq SC cluster, IBM SP, and Windows2000/XP workstation (2 to 4 CPUs in SMP) and can be used on Hybrid-computer SMP-DMP on a Linux cluster [*Pannala et al.*, 2003].

[67] All the "Fix-family" codes (e.g., K-FIX, MFIX, (G)MFIX) are property of the U.S. government through the Department of Energy (DOE). The MFIX codes can be freely accessed at http://

www.mfix.org. In the same vein, a similar code, CFDlib, may also be used for multiphase flow dynamic at http://www.lanl.gov/orgs/t/t3/codes/cfdlib.shtml.

Acknowledgments

References

Bouillard, J. X., D. Gidaspow, and R. W. Lyczkowski (1991), Hydrodynamics of fluidization: Fast-bubble simulation in a two-dimensional fluidized bed, *Powder Technol.*, 66, 107–118.

Boyle, E. J., W. N. Sams, and S. M. Cho (1998), MFIX validation studies: December 1994 to January 1995, *DOE/FETC-97/1042 (DE97002161)*, *CRADA PC94–026*, U.S. Dep. of Energy, Washington, D. C.

Branney, M. J., and P. A. Kokelaar (1992), A reappraisal of ignimbrite emplacement: Progressive aggradation and changes from particulate to non-particulate flow during emplacement of high-grade ignimbrite, *Bull. Volcanol.*, *54*, 504–520.

Calder, E. S., R. S. J. Sparks, and M. C. Gardeweg (2000), Erosion, transport and segregation of pumice and lithic clasts in pyroclastic flows inferred from ignimbrite at Lascar Volcano, Chile, *J. Volcanol. Geotherm. Res.*, *104*, 201–235.

Cas, R. A. F., and J. V. Wright (1988), *Volcanic Successions: Modern and Ancient*, 528 pp., Chapman and Hall, New York.

Dartevelle, S. (2003), Numerical and granulometric approaches to geophysical granular flows, Ph.D. dissertation thesis, Dep. of Geol. and Min. Eng., Mich. Technol. Univ., Houghton.

Dartevelle, S. (2004), Numerical modeling of geophysical granular flows: 1. A comprehensive approach to granular rheologies and geophysical multiphase flows, *Geochem. Geophys. Geosyst.*, *5*, doi:10.1029/2003GC000636, in press.

D'Azevedo, E., P. Sreekanth, M. Syamlal, A. Gel, M. Prinkley, and T. O'Brien (2001), Parallelization of MFIX: A multiphase CFD code for modeling fluidized beds, paper presented at Tenth SIAM Conference on Parallel Processing for Scientific Computing, Soc. for Ind. and Appl. Math., Portsmouth, Va.

Dobran, F., A. Neri, and G. Macedonio (1993), Numerical simulations of collapsing volcanic columns, *J. Geophys. Res.*, *98*, 4231–4259.

Druitt, T. H. (1998), Pyroclastic density currents, in *The Physics of Explosive Volcanic Eruptions*, edited by J. S. Sparks and R. S. J. Sparks, *Geol. Soc. Spec. Publ.*, *145*, 145–182.

Freundt, A., and M. Bursik (1998), Pyroclastic flow transport mechanisms, in *From Magma to Tephra: Modeling Physical Processes of Explosive Volcanic Eruptions*, edited by A. Frendt and M. Rosi, pp. 173–243, Elsevier Sci., New York.

Gidaspow, D. (1986), Hydrodynamics of fluidization and heat transfer: Supercomputer modeling, *Appl. Mech. Rev.*, *39*, 1–23.

Gidaspow, D. (1994), *Multiphase Flow and Fluidization: Continuum and Kinetic Theory Descriptions*, 467 pp., Academic, San Diego, Calif.

Guenther, C., and M. Syamlal (2001), The effect of numerical diffusion on isolated bubbles in a gas-solid fluidized bed, *Powder Technol.*, *116*, 142–154.

Harlow, F. H., and A. Amsden (1975), Numerical calculation of multiphase fluid flow, *J. Comput. Phys.*, *17*, 19–52.

Holasek, R. E., and S. Self (1995), GOES weather satellite observations and measurements of the May 18, 1980, Mount St. Helens eruption, *J. Geophys. Res.*, *100*, 8469–8487.

Holasek, R. E., A. W. Woods, and S. Self (1996), Experiments on gas-ash separation processes in volcanic umbrella plumes, *J. Volcanol. Geotherm. Res.*, *70*, 169–181.

Ishii, M. (1975), *Thermo-fluid Dynamic Theory of Two-Phase Flow*, 248 pp., Eyrolles, Paris.

Johnson, J. B. (2003), Generation and propagation of infrasonic airwaves from volcanic explosions, *J. Volcanol Geotherm. Res.*, *121*, 1–14.

Lakehal, D. (2002), On the modeling of multiphase turbulent flows for environmental and hydrodynamic applications, *Int. J. Multiphase Flow*, *28*, 823–863.

Mikumo, T., and B. A. Bolt (1985), Excitation mechanism of atmospheric pressure waves from the 1980 Mount St. Helens eruption, *Geophys. J. R. Astron. Soc.*, *81*, 445–461.

Morton, B. R., G. F. R. S. Taylor, and J. S. Turner (1956), Turbulent gravitational convection from maintained and instantaneous sources, *Proc. R. Soc. London, Ser. A*, *234*, 1–23.

Neri, A., and G. Macedonio (1996), Numerical simulation of collapsing volcanic columns with particles of two sizes, *J. Geophys. Res.*, *101*, 8153–8174.

Neri, A., A. D. Muro, and M. Rosi (2002), Mass partition during collapsing and transitional columns by using numerical simulations, *J. Volcanol Geotherm. Res.*, *115*, 1–18.

Neri, A., T. Esposti Ongaro, G. Macedonio, and D. Gidaspow (2003), Multiparticle simulation of collapsing volcanic columns and pyroclastic flow, *J. Geophys. Res.*, *108*(B4), 2202, doi:10.1029/2001JB000508.

O'Rourke, P. J., D. C. Haworth, and R. Ranganathan (1998), Three-dimensional computational fluid dynamic, *LA–13427–MS*, Los Alamos Natl. Lab., Los Alamos, N. M.

Pannala, S., E. D'Azevedo, M. Syamlal, and T. O'Brien (2003), Hybrid (OpenMP and MPI) parallelization of MFIX: A multiphase CFD code for modeling fluidized beds, paper presented at ACM SAC 2003, Assoc. for Comput. Mach., Melbourne, Fla.

Patankar, S. (1980), *Numerical Heat Transfer and Fluid Flow*, 197 pp., Taylor and Francis, Philadelphia, Pa.

Patankar, S., K. C. Karki, and K. M. Kelkar (1998), Finite volume method, in *The Handbook of Fluid Dynamics*, edited by R. W. Johnson, pp. 27-1–27-6, CRC Press, Boca Raton, Fla.

Press, W. H., B. P. Flannery, S. A. Teukolsky, and W. T. Vetterling (1986), *Numerical Recipes: The Art of Scientific Computing*, 818 pp., Cambridge Univ. Press, New York.

Rivard, W. C., and M. D. Torrey (1977), K-FIX: A computer program for transient, two-dimensional, two-fluid flow, *LA-NUREG-6623*, Los Alamos Natl. Lab., Los Alamos, N. M.

Rivard, W. C., and M. D. Torrey (1978), PERM: Corrections to the K-FIX code, *LA-NUREG-6623 Suppl.*, Los Alamos Natl. Lab., Los Alamos, N. M.

Rivard, W. C., and M. D. Torrey (1979), THREED: An extension of the K-FIX code for three-dimensional calculations, *LA-NUREG-6623 Suppl. II*, Los Alamos Natl. Lab., Los Alamos, N. M.

Rose, W. I., A. B. Kostinski, and L. Kelley (1995), Real-time C-band radar observations of 1992 eruption clouds from Crater Peak, Mount Spurr Volcano, Alaska, in *The 1992 Eruption of Crater Peak Vent, Mount Spurr Volcano, Alaska*, edited by T. E. C. Keith, *U.S. Geol. Surv. Bull.*, *2139*, 19–26.

Saad, Y., and M. H. Schultz (1986), GMRES: A generalized minimal residual algorithm for solving nonsymmetric linear systems, *SIAM J. Sci. Stat. Comput.*, *7*, 856–869.

Settle, M. (1978), Volcanic eruptions clouds and the thermal power output of explosive eruptions, *J. Volcanol. Geotherm. Res.*, *3*, 309–324.

Smagorinsky, J. (1963), General circulation experiments with the primitive equations: I. The basic experiment, *Mon. Weather Rev.*, *91*, 99–164.

Smagorinsky, J. (1993), Some historical remarks of the use of nonlinear viscosities, in *Large Eddy Simulation of Complex Engineering and Geophysical Flows*, edited by B. Galperin and S. A. Orszag, pp. 3–36, Cambridge Univ. Press, New York.

Spalding, D. B. (1981), Numerical computation of multiphase fluid flow and heat transfer, in *Numerical Computation of Multi-phase Flows*, *Lecture Series 1981–2*, edited by J. M. Buchlin and D. B. Spalding, von Karmán Inst. for Fluid Dyn., Rhode-Saint-Genèse, Belgium.

Spalding, D. B. (1983), Developments in the IPSA procedure for numerical computation of multiphase-flow phenomena with interphase slip, unequal, temperature, etc., in *Numerical Properties and Methodologies in Heat Transfer*, edited by T. M. Shih, pp. 421–436, Taylor and Francis, Philadelphia, Pa.

Sparks, R. S. J. (1986), The dimension and dynamics of volcanic eruption columns, *Bull. Volcanol.*, *48*, 3–15.

Sparks, R. S. J., and G. P. L. Walker (1977), The significance of vitric-enriched air-fall ashes associated with crystal-enriched ignimbrites, *J. Volcanol. Geotherm. Res.*, *2*, 329–341.

Sparks, R. S. J., L. Wilson, and G. Hulmes (1978), Theoretical modeling of the generation, movement and emplacement of pyroclastic flows by column collapse, *J. Geophys. Res.*, *83*, 1727–1739.

Sparks, R. S. J., M. I. Bursik, S. N. Carey, J. S. Gilbert, L. S. Glaze, H. Sigurdson, and A. W. Woods (1997), *Volcanic Plumes*, 574 pp., John Wiley, Hoboken, N. J.

Syamlal, M. (1994), MFIX documentation: User's manual, *DOE/METC-95/1013*, *DE9500,031*, 87 pp., U.S. Dep. of Energy, Washington, D. C.

Syamlal, M. (1998), MFIX documentation: Numerical technique, 80 pp., *DOE/MC/31346-5824*, *DE98002029*, U.S. Dep. of Energy, Washington, D. C.

Syamlal, M., W. Rogers, and T. J. O'Brien (1993), MFIX documentation: Theory guide, 49 pp., *DOE/METC-94/1004*, *DE9400,097*, U.S. Dep. of Energy, Washington, D. C.

Tahira, M., M. Nomura, Y. Sawada, and K. Kamo (1996), Infrasonic and acoustic-gravity waves generated by the Mount Pinatubo eruption of June 15, 1991, in *Fire and Mud: Eruptions and Lahars of Mount Pinatubo, Philippines*, edited by C. G. Newhall and R. S. Punonybanan, pp. 601–613, Univ. of Washington Press, Seattle.

Todesco, M., A. Neri, T. Esposti Ongaro, P. Papale, G. Macedonio, R. Santacroce, and A. Longo (2002), Pyroclastic flow hazard assessment at Vesuvius (Italy) by using numerical modeling. I. Large-scale dynamics, *Bull. Volcanol.*, *64*, 155–177.

Valentine, G. A., and K. H. Wohletz (1989), Numerical models of plinian eruption columns and pyroclastic flows, *J. Geophys. Res.*, *94*, 1867–1887.

Valentine, G. A., K. H. Wohletz, and S. Kieffer (1991), Sources of unsteady column dynamics in pyroclastic flow eruptions, *J. Geophys. Res.*, *96*, 21,887–21,892.

Van der Vorst, H. A. (1992), BI-CGSTAB: A fast and smoothly converging variant of BI-CG for the solution of nonsymmetric linear systems, *SIAM J. Sci. Stat. Comput.*, *13*, 631–644.

Walker, G. P. L. (1985), Origin of coarse lithic breccias near ignimbrite source vents, *J. Volcanol. Geotherm. Res.*, *25*, 157–171.

Wen, S., and W. I. Rose (1994), Retrieval of sizes and total masses of particles in volcanic clouds using AVHRR band 4 and 5, *J. Geophys. Res.*, *99*, 5421–5431.

Wilson, L., and J. W. Head (1981), Morphology and rheology of pyroclastic flows and their deposits, and guidelines for future observations, in *The 1980 Eruption of Mount St. Helens, Washington*, edited by P. W. Lipman and D. R. Mullineaux, *U.S. Geol. Surv. Prof. Pap.*, *1250*, 513–524.

Wilson, L., R. S. J. Sparks, T. C. Huang, and N. D. Watkins (1978), The control of volcanic column heights by eruption energetic and dynamics, *J. Geophys. Res.*, *83*, 1829–1836.

Woods, A. W., and C.-C. P. Caulfield (1992), A laboratory study of explosive volcanic eruptions, *J. Geophys. Res.*, *97*, 6699–6712.

Woods, A. W., and K. Wohletz (1991), Dimensions and dynamics of co-ignimbrite eruptions columns, *Nature*, *350*, 225–227.

Woods, A. W., and S. Self (1992), Thermal disequilibrium at the top of volcanic clouds and its effect on estimates of the column height, *Nature*, *355*, 628–630.

Zehner, P., and E. U. Schlunder (1970), Warmeleiftahigkeit von Schuttungen bei maβigen Temperaturen, *Chem. Ing. Tech.*, *42*, 933–941.

Zurn, W., and R. Widmer (1996), Worldwide observation of bichromatic long-period Rayleigh waves excited during the June 15, 1991, eruption of Mount Pinatubo, *Fire and Mud: Eruptions and Lahars of Mount Pinatubo, Philippines*, edited by C. G. Newhall and R. S. Punonybanan, pp. 615–624, Univ. of Washington Press, Seattle.